Bioactive Materials 14 (2022) 219–233

Contents lists available at ScienceDirect

Bioactive Materials

journal homepage: www.keaipublishing.com/en/journals/bioactive-materials

Multivalent network modifier upregulates bioactivity of multispecies biofilm-resistant polyalkenoate cement

Ji-Yeong Kim [a,b,1], Woojin Choi [c,1], Utkarsh Mangal [a,1], Ji-Young Seo [a], Tae-Yun Kang [d], Joohee Lee [e], Taeho Kim [c], Jung-Yul Cha [a], Kee-Joon Lee [a], Kwang-Mahn Kim [d], Jin-Man Kim [f], Dohyun Kim [g], Jae-Sung Kwon [b,d,*], Jinkee Hong [c,**], Sung-Hwan Choi [a,b,***]

[a] Department of Orthodontics, Institute of Craniofacial Deformity, Yonsei University College of Dentistry, 50-1 Yonsei-ro, Seodaemun-gu, Seoul 03722, Republic of Korea
[b] BK21 FOUR Project, Yonsei University College of Dentistry, 50-1 Yonsei-ro, Seodaemun-gu, Seoul 03722, Republic of Korea
[c] Department of Chemical and Biomolecular Engineering, Yonsei University, 50 Yonsei-ro, Seodaemun-gu, Seoul 03722, Republic of Korea
[d] Department and Research Institute of Dental Biomaterials and Bioengineering, Yonsei University College of Dentistry, 50-1 Yonsei-ro, Seodaemun-gu, Seoul 03722, Republic of Korea
[e] Johns Hopkins University, 3400 N. Charles St., Mason Hall, Baltimore, MD 21218, USA
[f] Department of Oral Microbiology and Immunology, School of Dentistry and Dental Research Institute, Seoul National University, Seoul 08826, Republic of Korea
[g] Department of Conservative Dentistry, Oral Science Research Center, Yonsei University College of Dentistry, 50-1 Yonsei-ro, Seodaemun-gu, Seoul 03722, Republic of Korea

ARTICLE INFO

Keywords:
Multivalent network modifier
Bioactive materials
Glass polyalkenoate cement
Ion release
Remineralization
Multispecies biofilm resistance

ABSTRACT

Polyalkenoate cement (PAC) is a promising material for regenerative hard tissue therapy. The ionically rich glass component of PAC encourages bioactive interaction *via*. the release of essential ions. However, PAC bioactivity is restricted owing to (i) structurally inherent cationic network formers and (ii) surface bacterial biofilm formation. These two factors cause a deficiency in ion release, further complicated by secondary infections and premature therapeutic failure. Here, a multivalent zwitterionic network modifier (*m*ZM) is presented for upregulation of ionic exchange and bioactivity enhancement. By introducing a non-zero charged *m*ZM into PACs, an increase in the proportion of non-bridging oxygen occurs. The network modification promotes ion channel formation, causing a multiple-fold increase in ion release and surface deposition of hydroxy-carbonate apatite (*ca*. 74%). Experiments *ex vivo* and animal models also demonstrate the efficient remineralization ability of the *m*ZM. Furthermore, divalent cationic interaction results in bacterial biofilm reduction (*ca*. 68%) while also influencing a shift in the biofilm species composition, which favors commensal growth. Therefore, PAC modification with *m*ZM offers a promising solution for upregulation of bioactivity, even aiding in customization by targeting site-specific regenerative therapy in future applications.

1. Introduction

Aging, disease, and trauma-related conditions have long driven the research focus on regeneration and remineralization of dental and bone tissues [1–3]. The development of novel bioactive materials has been one of the key concerns in addressing the needs of regenerative therapies. Bioactivity, a fundamental principle in biomaterial regenerative therapy, has been described in several ways, including (i) non-fibrous bonding to the mineralized tissue such as bone and (ii) aiding the synthesis of bio-inherent material such as hydroxy-carbonate apatite (HCA) [4,5]. Glass polyalkenoate cement (PAC), in accordance with the above definition, has been often highlighted as the 'gold

Peer review under responsibility of KeAi Communications Co., Ltd.
* Corresponding author. Department and Research Institute of Dental Biomaterials and Bioengineering, Yonsei University College of Dentistry, 50-1 Yonsei-ro, Seodaemun-gu, Seoul 03722, Republic of Korea.
** Corresponding author. Department of Chemical and Biomolecular Engineering, Yonsei University, 50 Yonsei-ro, Seodaemun-gu, Seoul 03722, Republic of Korea.
*** Corresponding author. Department of Orthodontics, Institute of Craniofacial Deformity, Yonsei University College of Dentistry, 50-1 Yonsei-ro, Seodaemun-gu, Seoul 03722, Republic of Korea.
E-mail addresses: jkwon@yuhs.ac (J.-S. Kwon), jinkee.hong@yonsei.ac.kr (J. Hong), selfexam@yuhs.ac (S.-H. Choi).
[1] These authors contributed equally to the article.

https://doi.org/10.1016/j.bioactmat.2021.11.020
Received 20 August 2021; Received in revised form 25 October 2021; Accepted 15 November 2021
Available online 20 November 2021

standard' for therapeutic applications encompassing the diverse fields of dentistry, neuro-otology, and orthopedics (Fig. 1A) [6,7].

PAC composite cement is the derivative of a reaction between glass (powder phase) and poly acids (aqueous phase). The dual-action glass phase serves as a filler and reactionary source of cations. The characteristic acid–base reaction of PAC involves the hydrolytic rupture of the bridging oxygens (BOs) in the glass structure *via.* surface aqueous gelation [7]. The subsequent maturation stage features the release of cations (*e.g.*, Ca^{2+} and Al^{3+}) that crosslink with the polyalkenoate groups resulting in a polysalt matrix formation, ending with the formation of a silica gel layer around the glass particles [8]. This ionically rich reaction favors the bio-interactive interface, allowing PACs to covalently bond with the hard tissue [9]. The bulk of PAC contains glass particles as a reservoir of bioactive ions (*i.e.*, inducerons), which release on interaction with body fluids to stimulate effective blending of the cement–tissue interface, subsequently reducing the interfacial failure. The bioactive effect induces an active ionic interaction with the surrounding hard tissues.

However, *in vivo* studies in the past have drawn attention to the contentious nature of Al^{3+}, with osteomalacia (defective mineralization) being reported [10–12]. Multiple studies have attempted substituting Al^{3+} with other cations to alter the core glass formulation of PAC to mitigate mineralization-related side-effects [13]. Amongst the cations, Zn^{2+} has been particularly favored being an essential trace element. In low doses, Zn^{2+} is known to improve cellular activation, which promotes hard-tissue mineralization. However, a total substitution of Al^{3+} with Zn^{2+} can substantially reduce the mechanical performance by reducing crosslinking with polymeric chains [7,14]. While Al^{3+} is a network intermediate, Zn^{2+} is predominantly a network former with only a mild network modifying action. Thus, with its strong 4-fold coordination, Zn^{2+} favors a more robust BO network, which resists interfacial exchange of inducerons and subsequently limits bioactivity [15].

In addition, the bioactivity of PACs is also hampered by the surface planktonic attachment [16]. Protein-rich adhesion limits the ionic exchange by forming a diffusion barrier and is believed to cause premature termination of HCA formation [17]. Furthermore, the PAC surface is

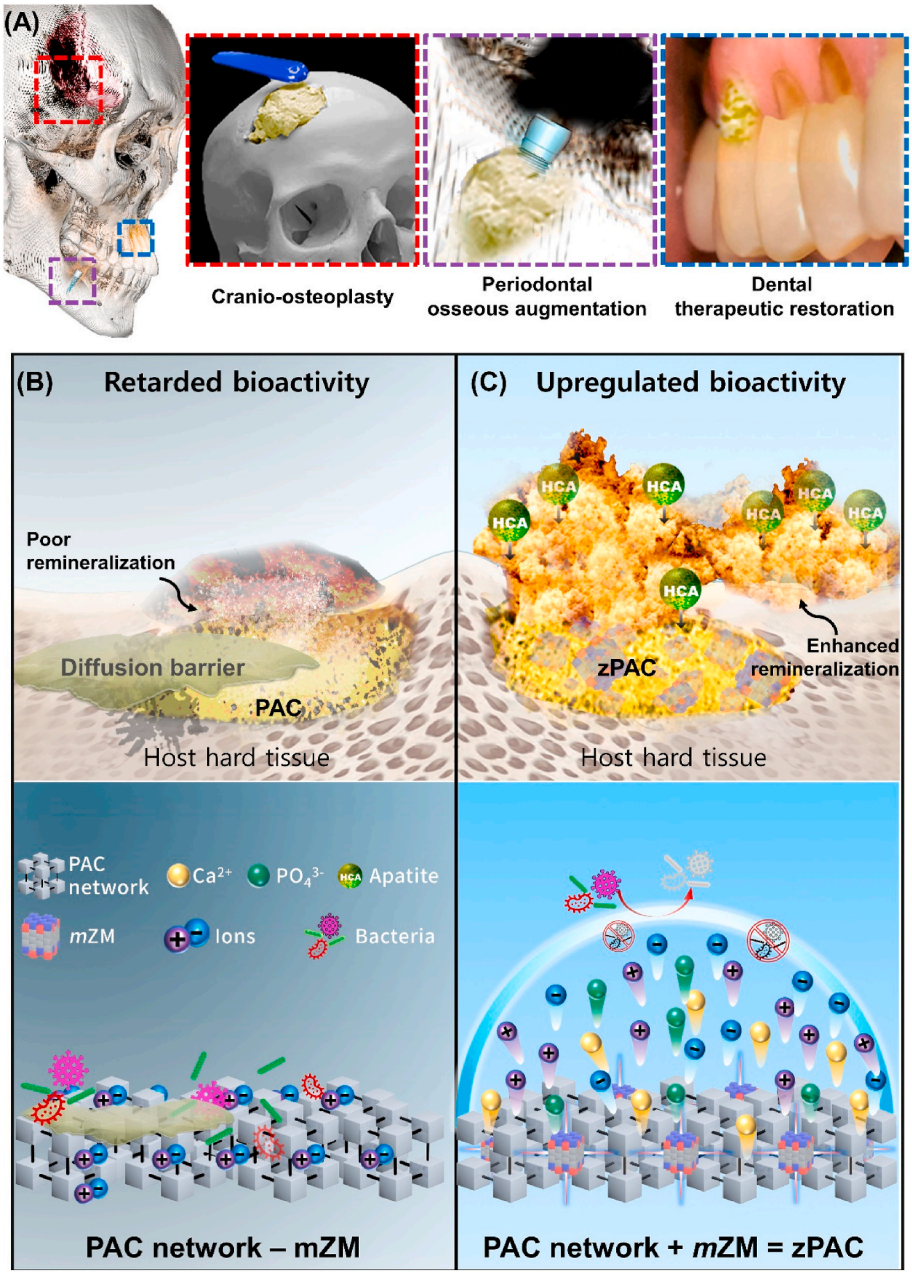

Fig. 1. Schematic representation of biomedical application of dual action zPAC and ultrastructural effect of *m*ZM. (A) Therapeutic applications of the zPAC (yellow cementitious) in treatment of craniosskeletal traumatic defects, periodontal bone loss associated problems, and direct restoration of cavitated and demineralized regions of the tooth. (B–C) Mechanism of comparison at ultrastructure level between (B) PAC and (C) zPAC as a factor of multivalent zwitterionic network modifier (*m*ZM). The zPAC binds and blends with the host hard tissue by forming hydroxy-carbonate apatite (HCA) facilitated by the *m*ZM action. *m*ZM upregulates bioactivity of the zPAC by improving the release of ions by increasing the proportion of non-bridging oxygen.

susceptible to secondary infection in a multispecies microbial environment and becomes predisposed to interfacial failure in the hard tissues, leading to a premature therapeutic loss [18]. Hence, a bifactorial etiology causes retardation of bioactivity from the PACs (Fig. 1B).

Herein, we propose introducing a programmable multivalent network modifier, comprised of zwitterionic derivatives (Methacryloyloxyethyl phosphorylcholine (MPC) and sulfobetaine (SB) [19,20]), in the PAC to (i) upregulate the bioactivity by improving ionic exchange through microstructural network changes and (ii) impede planktonic diffusion barrier formation (Fig. 1C). We successfully generated zPAC, *i.e.,* PAC incorporating zwitterionic modifiers (ZMs). The role of multivalent network modifiers was investigated by comparing the ion release and its impact on the submersion media chemical profile. The net charge of the combined state and ratio of bridging oxygen/non-bridging oxygen (BO/NBO) has been discussed further, which may have consequently affected the ion release of inducerons.

Furthermore, we successfully validated the substantial augmentation in bioactivity with zPAC by eliciting (i) multiple-fold increase in the release of key inducerons (Zn^{2+}: *ca.* 240, Ca^{2+}: *ca.* 40, Sr^{2+}: *ca.* 51, and PO_4^{3-}: *ca.* 130), (ii) increased *in vitro* HCA deposition: *ca.* 75%, and (iii) marked multispecies biofilm resistance: *ca.*68%. We could also observe an excellent HCA formation aiding remineralization, indicating efficient bioactivity upregulation of zPAC, presented *via. ex vivo* and *in vivo* models.

2. Results and discussion

2.1. Structural envisioning of bioactive PACs as a function of zwitterionic network modifier

The amounts of ZMs were predetermined based on previous studies, demonstrating a negligible deterioration of clinically relevant physical and chemical properties [19–23]. Specifically, the zwitterionic amphiphiles were regarded as the anomalous network modifier to govern the ion release kinetics from the intrinsic oxygen network of PAC. In

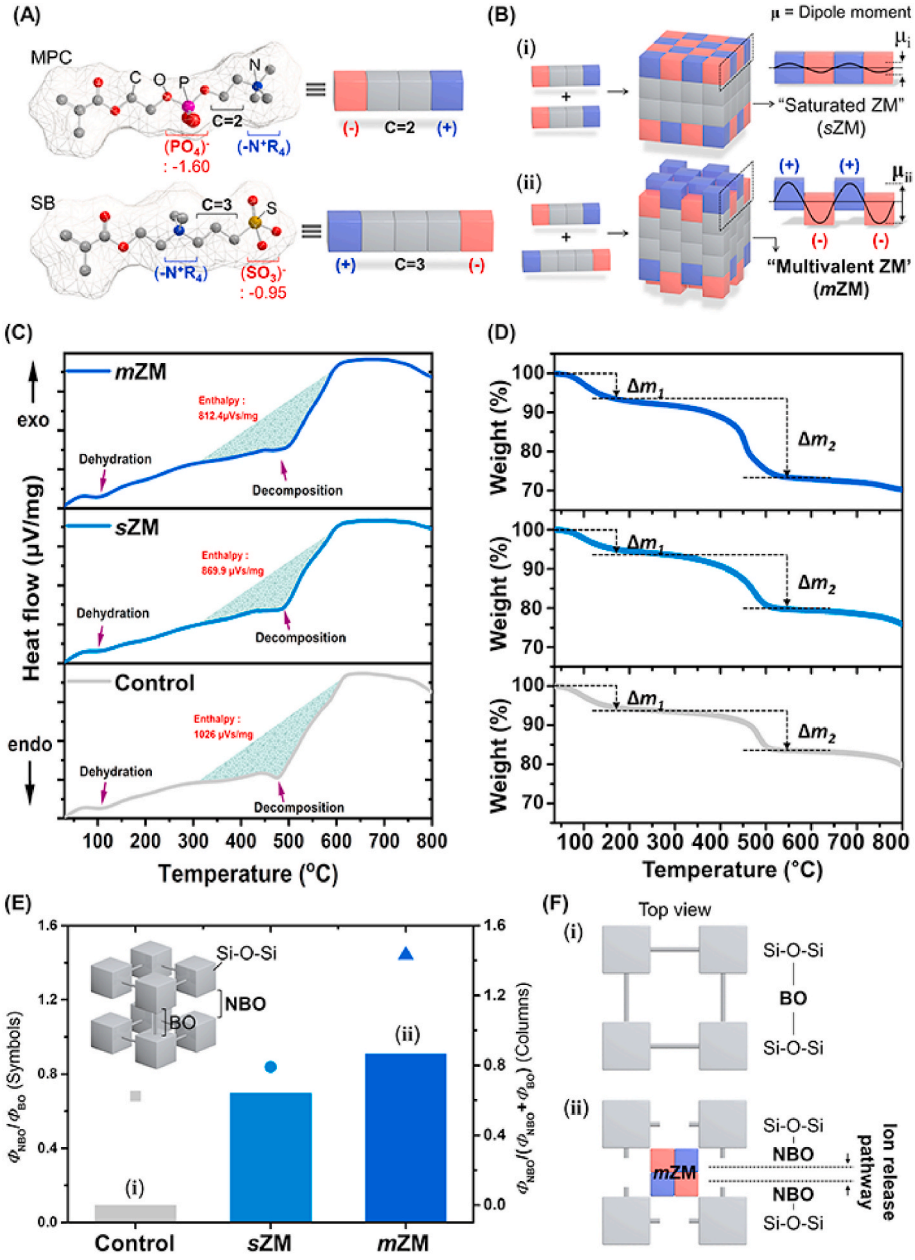

Fig. 2. Structural envisioning of PAC with multivalent zwitterionic modifiers. (A) The zwitterionic derivatives (MPC, SB) are represented as Tetris blocks. The blocks feature the charge (blue/red) and carbon length (grey). (B) Schematic illustrating the representative zwitterionic modifiers (ZMs) in terms of the number of elements. The selection of zwitterionic elements resulted in the different ZMs; that is, B-i) saturated ZM (*s*ZM) and B-ii) multivalent ZM (*m*ZM). The symbol μ indicates the dipole moment. (C–F) Multilateral quantifications of NBO portions (Φ_{NBO}). (C) DSC spectra of PACs. (D) TGA spectra of PACs. The solid lines from the bottom sequentially indicate Control, *s*ZM, and *m*ZM. (E) Summarized Φ_{NBO} of PACs originating from Raman spectroscopy and XPS. F) Schematic illustration (i) represents BO structure of Control, and (ii) corresponds to NBO structure induced by *s*ZM and *m*ZM. Here, BO: bridging oxygen, NBO: non-bridging oxygen.

general, the cationic network modifier (*e.g.,* Na^+, Ca^{2+} ions) electrostatically interacted with the bridging oxygen (BO, Si–O–Si), leading to non-bridging oxygen (NBO, Si–O) and a corresponding ion release channel [7]. Note that the NBO portion (Φ_{NBO}) is positively tangled with the ion release profile of PACs [24].

Zwitterionic amphiphiles prefer to aggregate because of the interactions among anions and cations [25]. The single zwitterionic element conforms to the zero-charged aggregate (*e.g.,* micelles, vesicles), counterbalancing the opposite charges [26]. Previous studies have introduced external reagents (*e.g.,* salts, polyelectrolytes) to deconstruct the less active zero-charged geometry [27]. In this study, the tractable conjugation within the zwitterion library featured the programmable activity of ZM.

The net charge of unit zwitterionic amphiphiles converges to zero within two isoelectric points [28]. However, the varying carbon lengths resulted in considerable variation between partial charges of anionically charged moieties; that is, −1.5952 for $(PO_4)^-$ of MPC and −0.9537 for $(SO_3)^-$ of SB (Fig. 2A). The corresponding asymmetry of partial charges (*i.e.,* charge asymmetry) could parameterize the geometries of ZM (Fig. 2B) [29]. The homogeneous Coulombic force is spontaneous within the charged groups of symmetric intensity. Hence, the unitary zwitterionic system could aggregate to the saturated ZMs (*s*ZM) featuring the zero net charge and narrow dipole moment (Fig. 2B-i).

Alternatively, the asymmetric charged groups of diverse intensity could guide the non-zero charged aggregate retaining the anomalous Coulombic forces. Hence, the substantial difference between anionic partial charges could result in a more active geometry of ZMs, *i.e.*, the so-called multivalent ZM (*m*ZM) (Fig. 2B-ii) [30–32]. Here, the activity of ZM represents the proportional dipole moment to deconstruct the BO network. The dipole–dipole interaction triggered by ZM could disturb the BO network and guide the elevated values of Φ_{NBO}. *m*ZM might favorably influence Si–O–Si conformation. The geometrical differences of ZMs and corresponding variation of intrinsic PAC structure were empirically addressed as follows.

The diverse Si–O–Si networks were monitored during the thermal analysis as a function of ZMs (Fig. 2C and D). A general decrease occurred in decomposition enthalpy with the addition of ZMs; that is, *s*ZM (15.21%) < *m*ZM (20.82%) in Fig. 2C. The endothermic peaks occurring around 100 °C are responsible for dehydration, indicating the evaporation of residual moisture contained in the material. In comparison, the second endothermic peak (*ca.* 500 °C) could be attributed to carboxylic acid decomposition [33,34]. Two noticeable weight reductions emerged; that is, Δm_1 (30–200 °C) and Δm_2 (300–600 °C) as in Fig. 2D. Δm_1 and Δm_2 denote the evaporation of residual water and decomposition of BO network, respectively. The amount of residual water (Δm_1) was highest in *m*ZM (Figure S1A). Further investigations (*i.e.,* Raman spectroscopy and water uptake amounts in Figure S2) featured sufficient hydration ability by the introduced ZMs. Furthermore, the decomposition of BO (Δm_2) was enhanced in the order Control (10.1%) < *s*ZM (12.6%) < *m*ZM (18.7%) (Figure S1B), confirming that the BO network was loosened owing to the active *m*ZM.

X-ray photoelectron spectroscopy (XPS) and Raman measurements were performed to monitor the Si–O–Si network, confirming that the active *m*ZM sufficiently enhanced Φ_{NBO} (Figure S3). In Figure S3A, Control presented the unapparent NBO-related peaks of Si–O–2NBO (~965 cm^{-1}) and Si-O-NBO (~1035 cm^{-1}). Notably, the aforementioned peaks increased as ZMs were introduced; in particular, they were maximized when the active *m*ZM was adopted.

95% of electron binding energies within 10 nm of the outermost surface were achieved through XPS [35]. Specifically, N_{1s} spectrum was rigorously investigated because the cationic functional group ($-N^+R_4$) of ZMs was the primary dipole interaction spot with BO. In Figure S3B, zPACs solely presented the significant peaks. The protonated amine ($-N^+R_4$) peaks at 402.3 eV distinctly weakened as ZMs were introduced. Here, the protonated amine ($-N^+R_4$) of ZMs became uncharged owing to the deportation (*i.e.,* dipole–dipole interaction with BO, forming Si–O–N). As proof of our hypothesis, *m*ZM effectively modified the Si–O–Si network, boasting the negligible charged amine spectrum. Noticeably, zPACs featured a higher level of residual Φ_{NBO} after the sufficient ion release (Figure S3C). The details of ion release are described in the following sections.

The relationship between the activity of ZMs and Φ_{NBO} was summarized in Fig. 2E. The empirical values indicated that ZM strongly governed Φ_{NBO}. Specifically, *s*ZM still afforded the innovative network modification. Furthermore, the active geometry of *m*ZM considerably disturbed the original BO structure and guided the formation of the additional pathway of ion release (Fig. 2F).

2.2. Elution of inducerons and assay of biological activity in vitro

We conducted *in vitro* evaluation to validate the aforementioned changes in the structural characteristics under the impact of ZMs. The nature of the biological response is guided by the constituent ions of the glass component in the PACs [4]. We studied the PAC composed of fluoroalumiosilicate and fluorozincsilicate glass parts. The ionomeric cement first proposed by William and Kent was thoroughly investigated for characteristic fluoride release [36]. The fluoride release mitigates further hard tissue deprivation and aided the remineralization of dental hard tissue. The bioactive component for application in bone repair contributed to the calcium-phosphate-rich compound formation at the PAC–bone interface [9]. Additional fluorozincsilicate filler was intended to further the bioactive response by deterring microbial growth and eliciting osteoconduction under the influence of Zn^{2+} [37,38]. The ionically rich PAC glass network interacts with the immediate environment (aqueous), facilitated by internal mobility and exchange of ions [8]. Such an interaction, central to the bioactivity of the glass–PACs, was therefore explored to test the modified network. Elution of ions including fluoride, zinc, sodium, calcium, phosphate, and strontium ions, after static incubation of 24 h in distilled water, was distinctly higher with *m*ZM (Fig. 3A).

Homeostasis of hard tissue modeling is closely related to the ambient pH, such that reduction from critical pH can cause unfavorable loss of mineral content. The critical pH for the dental hard tissues is believed to be at 5.5, below which the organic matrix begins to break and initiate demineralization. Similarly, for the deeper tissues at the periosteal level, slight pH changes can affect the healing and mineralization by affecting the cell activity [39]. We tested the buffering capacity (in lactic acid: pH = 4.0) of the Control against the zPACs in triplicate and observed that zPAC had a more steady change in pH. When comparing the buffering action between the three groups, Control and *s*ZM showed a rapid buffering (*s*ZM > Control) of the lactic acid pH, which peaked (*ca.* 5.2) within 60 min. In noteworthy contrast, the *m*ZM displayed a steady increase in pH, which peaked and stabilized well above the critical pH value in *ca.* 120 mins. The pH value for the *m*ZM remained appreciably above the threshold with little variation, in contrast to *s*ZM and Control groups displaying a reducing slope of pH–time curve with fluctuations (Fig. 3B).

Furthermore, we detailed the ion elution behavior over 21 days for the key inducerons (Fig. 3C and Figure S4). The elution behavior (with solution refreshing at regular intervals) showed the release pattern similar to findings from earlier studies [40]. The observation of release profile suggested an initial rapid release followed by reduction to a plateau after 72 h. A close to total release around day 7 followed by reduction below the detection level while nearing two-weeks was observed. While the zPACs showed detectable levels with low relative standard deviation, the cumulative ion concentration in the Control group after day 14 was at negligible detection levels. Particularly, calcium and phosphate cumulative concentration showed a significantly higher concentration at all measurement points after day 1. Significantly ($p < 0.01$) higher calcium concentration in *m*ZM elutes than *s*ZM was also observed on day 3 and day 7. However, phosphate concentration was statistically higher ($p < 0.05$) for *s*ZM compared to both *m*ZM and

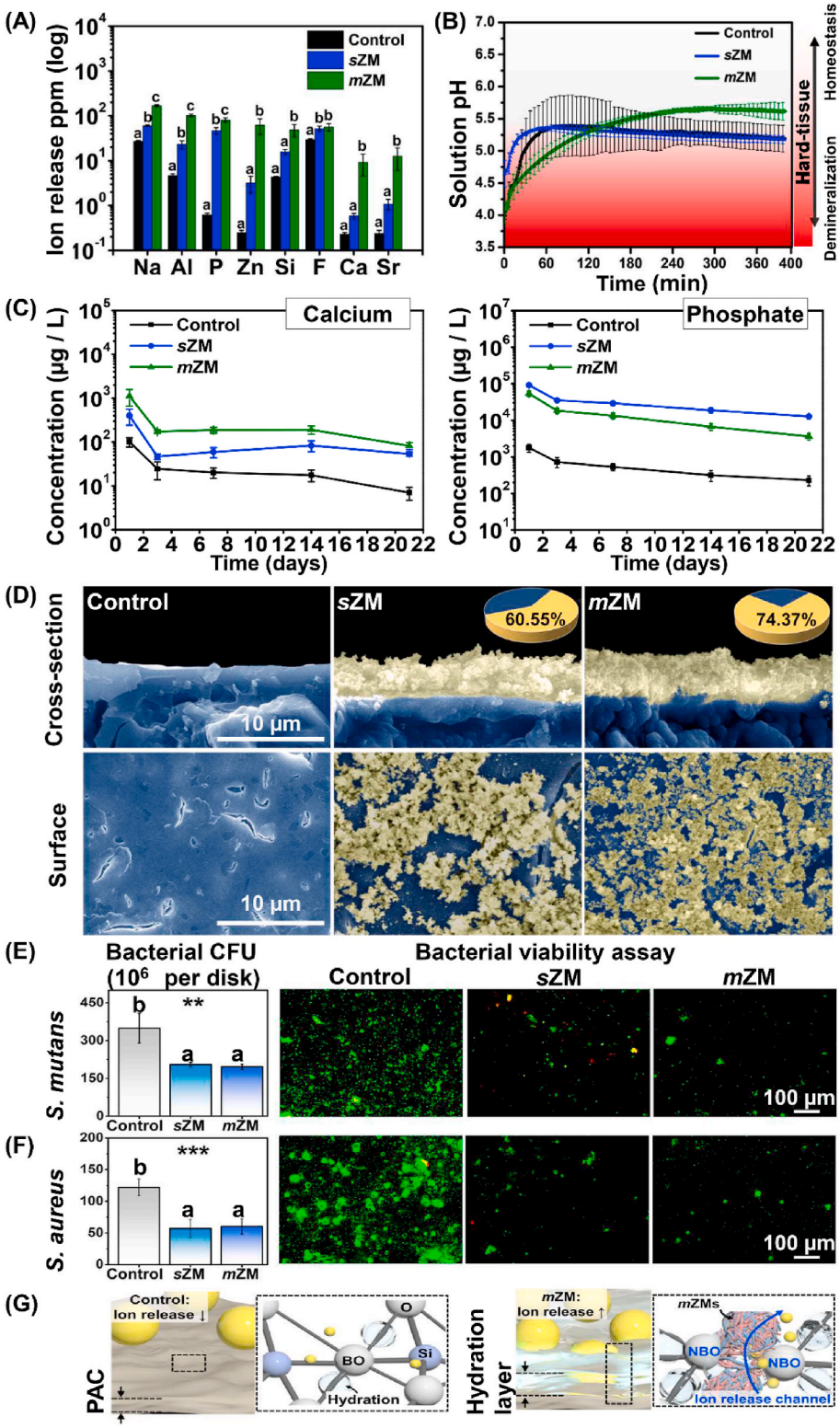

Fig. 3. Course of experiments and analyses *in vitro*. (A) Ion release from Control and zPAC specimens immersed in distilled water (n=3; $p < 0.05$). (B) Dynamic pH neutralization behavior of Control and zPAC as a factor of hard tissue homeostasis in lactic acid with an initial pH of 4.0 (n=3). (C) Elution of the inducerons, calcium and phosphate examined with spectrometry analysis of the elute performed at 1, 3, 7, 14 and 21 days, following submersion in distilled water. At least three replicates were analyzed. Additional inducerons evaluated are detailed in Figure S4 and the day-wise statistical evaluation using one-way ANOVA for threshold p value of 0.05 are tabulated in Table S1 through S5. Minimum of three replicates were analyzed at all time points. Y-axis log10 scale of cumulative concentration of the ions in μg/L. (D) Cross-section and surface SEM micrographs of Control and zPAC specimens showing apatite nucleation and growth after immersion in simulated body fluid for seven days. Pseudo-colored micrographs contrast the apatite-like precipitates (yellow) and the specimen surface (blue). Relative area (percentage) occupied by apatite in relation to the entire surface is expressed in the pie chart (inset) in the cross-section column of the respective groups. Scale bar is 10 μm. (E–F) Bacterial resistance of the Control and zPACs. Colony-forming unit (CFU) and the live and dead confocal microscopy imaging of *Streptococcus mutans* (E) and *Staphylococcus aureus* (F). Scale bar is 100 μm. (G) Suggested mechanism of Φ_{NBO}, ion release profile, and hydration dynamics for Control (left), and following the introduction of *m*ZM (right) in PAC. Statistical analysis such as one-way ANOVA and posthoc analysis of Tukey's test was conducted, with the difference in lowercase letters indicating significant differences (n=3, $^{**}p<0.01$, $^{***}p<0.001$).

Control for all measurement points. Table S1 through table S5 detail the day-wise comparison between the three groups for different ions released.

The difference in elution and subsequent changes in the immediate microenvironment influences the biochemical response of the biomaterial, such that incubation in a solution with an ionic profile like human blood plasma can elicit a bioactive response. Subsequently, the *in vitro* bioactivity test is exemplified by surface deposits of calcium-phosphate-rich apatite-analogs (*i.e.* HCA) [41]. We compared the Control and zPACs in the simulated body fluid (SBF; Table S6). After the first 24h interval, no apatite formation could be detected on the specimen surface (Figure S5); however, a layer of micro-spherical HCA deposits was observed after seven days of immersion. The seven-day SEM surface and cross-section micrographs showed a markedly higher percentage of mineralized precipitates in zPACs, detectably higher in the *m*ZM group (*ca.* 74%) (Fig. 3D).

A synergistic impression of augmented ion release and pH neutralizing effect could be elicited in the extraordinary bacterial resistance by zPACs. Extracellular polymeric substances influence the microenvironment of the biofilm by affecting porosity, density, charge, and sorption properties [42]. Divalent ions bind to extracellular substances' negatively charged functional groups and change their overall structure and function [43,44]. Hence, it is likely that the interaction with the divalent ions released in this study (Ca^{2+}, Zn^{2+}, and Sr^{2+}) complemented the bacterial resistance effect.

Streptococcus mutans and *Staphylococcus aureus* are etiologically classified as pathogenic for diseases of mineralized tissue in dental and skeletal tissues, respectively [45,46]. The two gram-positive bacteria were selected as the representative pathogens to evaluate the bacterial resistance of the PACs. Quantification of bacterial resistance of the zPACs was determined using confocal imaging, contrasting optical density (OD), and measurement of colony-forming units (CFUs). The zPACs showed considerable bacterial resistance observed as a superlative reduction in the OD and CFU counts compared to the Control. Bacterial resistance was markedly observed for representative bacteria *S. mutans* (Fig. 3E; $p < 0.01$) and *S. aureus* (Fig. 3F; $p < 0.001$) through reductions in colony growth. Imaging the live/dead bacteria further affirmed the enhanced resistance to bacterial adhesion, standing in sharp contrast to the Control group, which displayed dense attachment regions of green-stained live bacteria. A similar trend for resistance to adhesion was observed for *S. mutans* and *S. aureus*. However, qualitatively, relatively stronger resistance to *S. mutans* could be perceived in OD measurements (Figure S6A) and fluorescent microscopic imaging. Furthermore, in comparison to Control, the growth of *S. aureus* cultures in BHI was significantly ($p < 0.001$) inhibited in the *m*ZM group (Figure S6B).

Hence, we concluded that (i) *m*ZM effectively modifies the BO network to NBO, (ii) the ions are released out through the NBO-induced ion channel (Fig. 3G), (iii) hydroxyl-apatite formation is facilitated (Figure S7) and (iv) an effective surface bacterial resistance is demonstrated.

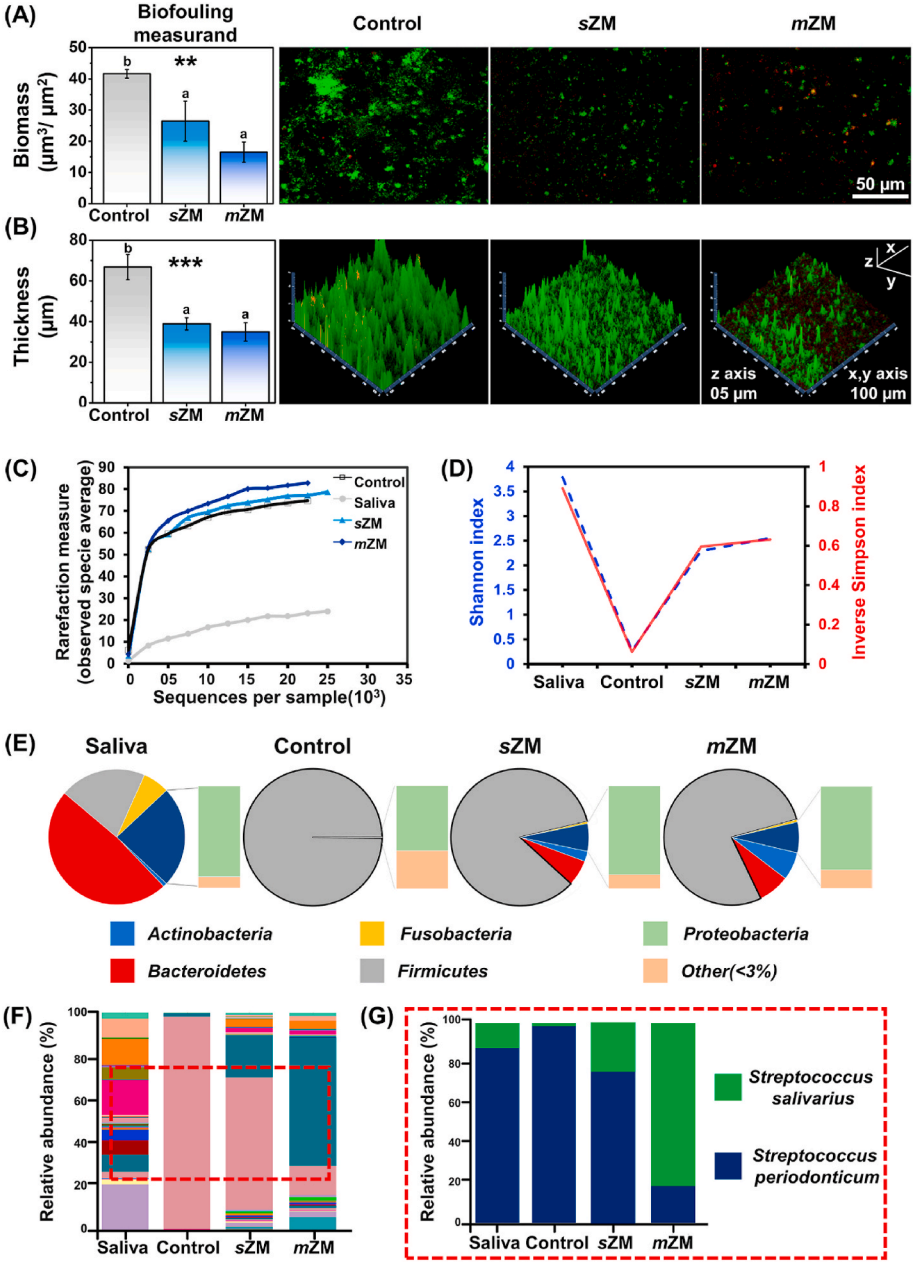

Fig. 4. Enhanced multispecies salivary biofilm resistance and improved ecological diversity balance of zPAC. (A–B) Multispecies biofouling resistance of the zPACs shows significant measurands reductions, (A) biofilm mass per unit area, and (B) biofilm thickness. Confocal image of the biofilm formed over the sample. Scale bars, 50 μm. The side-view image scale is 100 μm (x- and y-axes) and 20 μm (z-axis). Statistical analysis was carried out by one-way ANOVA and posthoc analysis of Tukey's test, with a difference in lowercase letters indicating significant differences (n=3, $^{**}p < 0.01$, $^{***}p < 0.001$). (C–G) Depiction of representative diversity of microbiome composition from sampled human saliva before and after culture with PAC specimens. (C) Ecological rarefaction measure curve to show species diversity between saliva and the biofilm over the PAC specimens. (D) Shannon and inverted Simpson diversity index comparative plot for various test groups. (E) Relative abundance of individual taxa per group summarized at the phylum level. F) Taxonomic composition for each sample at species level (x-axis: sample name; y-axis: operational taxonomic unit (OTU) proportions in relative abundance percentage. See Figure S8 for a detailed description of the various OTUs identified. (G) Composition analysis for abundance distribution of known commensal (*Streptococcus salivarius*) versus periodontal pathogen (*Streptococcus periodonticum*) observed between the PACs.

2.3. Resistance of zPACs to salivary multispecies pathogenic biofilm formation ex vivo

We conducted the *ex vivo* analysis in a clinically relevant setup with the help of multi-species human saliva [47]. The dental plaque biofilm is a complex microbiome housing more than 10^8 cells g^{-1} wet weight and over 700 prokaryote species [48]. The pathogenic state of dental tissue (enamel/dentin) demineralization occurs as a sequelae to shift in the internal equilibrium of plaque biofilm on the surface.

The zPACs displayed an extensive reduction in bacterial biofilm surface adhesion. In comparison to Control, an outstanding reduction in the measurands of biofilm mass (*s*ZM: *ca.* 37%, *m*ZM: *ca.* 68%; $p < 0.01$) and biofilm thickness (*s*ZM: *ca.* 42%, *m*ZM: *ca.* 48%; $p < 0.001$) was observed with the zPACs. Confocal imaging of the external micro surface reflected an analogous picture with a pronounced densely bright green staining of the Control group in strong contrast to the *m*ZM group with scanty and shallow lining of the stained biofilm region (Fig. 4A and B).

Interventions with PACs and other materials aid in treating the lesion locally, but reports of recurrence have drawn attention towards a critical need to prevent biofilm formation by explicitly targeting the responsible microorganisms [49]. The present study results are particularly encouraging when the refractory nature of the biofilm-associated periapical and periodontal bone loss is considered [50].

For evaluating the impact of the zPAC groups on the constituent microbiota, we adopted the high-throughput approach (16S metagenomic sequencing) to map the ecological rarefaction and the associated operational taxonomic unit (OTU) proportions. To analyze the comprehensiveness, we contrasted the changes between the groups using an untreated sample of saliva, free from the influence of PACs. Studying the diversity of the biofilm species, the rarefaction curves for the number of species observed showed a close resemblance between *s*ZM, *m*ZM, and saliva. In contrast, the Control group showed the lowest average before plateauing (Fig. 4C). To further analyze the bacterial diversity, Shannon and inverse Simpson indices were plotted (Fig. 4D). The Shannon index for bacterial richness reaffirmed the observation of the rarefaction curve with a similar ecological response observed for various zPACs. The independent saliva sample showed the highest Shannon and inverse Simpson index values, followed by the *m*ZM and the *s*ZM group, while the Control group showed the lowest.

Furthermore, the plaque microbiota displays a dynamic nature such that saturation of plaque biomass does not indicate the definitive state of the microbiota succession. Note that a complete absence of plaque formation on synthetic materials is unrealistic. Thus, an improved balance between the acidogenic bacteria and co-colonizer can favor the development of a healthy plaque with lower pathogenic predilection [51].

We studied the 48 h biofilm diversity at the phylum and species level, permitting comparison of difficult-to-grow organisms. A dominant proportion of the *Firmicutes* in the PACs was observed, in sharp contrast to saliva where *Bacteroidetes* comprised a more substantial proportion (Fig. 4E). The *Firmicutes* were dominated with *Streptococcaceae,* with the highest concentration recorded in Control (98.37%), followed by *s*ZM (79.83%) and *m*ZM (72.04%). The pristine salivary biofilm with a high diversity and evenness showed a relatively well-distributed proportion. The details are provided in the Supplementary Data (Table S7, Figure S8).

When comparing species-specific diversity, zPACs showed a general increase in the diversity of bacterial species (Fig. 4F). The more diverse the bacterial species in the oral cavity, the lower the prevalence of oral diseases [52]. Of particular interest was *Streptococcus* sp. distribution (Fig. 4G). The relative distribution of *Streptococcus periodonticum* to *Streptococcus salivarius* was exceptionally reduced for *m*ZM. The aforementioned distribution behavior affirms the modifying influence of the biomaterial on the oral microbiome. The reduction of *S. periodonticum,* the etiologic species for periodontitis [53], implies a complimentary protective action from the *m*ZM, favoring deeper surface lesion therapeusis in bone and tooth. Furthermore, an increased proportion of *S. salivarius* competitively inhibits biofilm formation under a probiotic-like action, hindering the growth of *S. mutans.* [54].

2.4. Ex vivo bioactive remineralizing effect of mZM

In vitro analysis of the *m*ZM showed a remarkable capacity for surface nucleation and apatite analogue formation on the cement surface following SBF immersion. We also characterized the elution of the Control and zPAC, and successfully demonstrated the cytocompatibility of *m*ZM using Human gingival fibroblasts (HGF-1) (supplemental methods and Figure S9). Furthermore, inferring from the results of preceding tests, an outstanding dual action (bioactivity + multispecies biofilm resistance) effect of *m*ZM could be concluded. Therefore, subsequent *ex vivo* and *in vivo* (see next section) tests were planned to compare Control and *m*ZM.

Corroborating the bioactive potency with a functionally relevant model, two *ex vivo* analyses were conducted in parallel, as illustrated in Figure S10. Targeting the principally established application of the PACs as a tooth restorative material, we simulated an enamel surface remineralization model (Figure S10A) with bovine teeth and an active dentin-bonded remineralization model (Figure S10B) using extracted human-premolar teeth. The remineralization potential was assessed for a total period of 14 days for *ex vivo* experiments. The conditions were factored from the long-term ion elution *in vitro* analysis. The valuation of cumulative ionic concentration could be elicited repeatedly only for 14 days of immersion in the Control group. Thus, with the possibility of the Control group being the limiting factor, the experiments were limited to 14 days of remineralization treatment.

In the first of the *ex vivo* test series, the enamel surface was initially demineralized by simulating *S. mutans* biofilm aciduric environment and then remineralized by passive approximation of the PAC discs. The de- and remineralization protocols were adapted from previous studies confirming the reproducibility of the same [55,56]. Alkaline conditions being more conducive to the formation of mineralized bone-like apatite [57], the remineralization steps were begun with SBF solution pH set at 7.4 (simulating the vascularized tissue pH).

The *m*ZM group under the credible effect of the ZMs showed a remarkable capacity to induce surface remineralization by forming multiple dense islands like deposits of HCA compounds. The demineralized enamel surface characterized with widened interrod spaces (Fig. 5A, green arrows at 5000 ×) and roughened surface topography could be contrasted against the *m*ZM group showing a smooth layer of deposits on the surface with the majority of the interrod areas obliterated under the remineralization influence following HCA deposits (Fig. 5A; yellow dotted outline). The Control group also showed faint signs of remineralization. The red arrows in Fig. 5A inset highlight the differences in the obliteration of demineralized interrod spaces.

Change in the SBF pH during the experiment was measured within a 24 h interval. The pH of the SBF solution (Fig. 5B) decreased swiftly for Control and *m*ZM groups up to the first 72 h and then increased gradually. The pH decreased from 7.44 to 6.63 and 7.44 to 6.58 for the Control and the *m*ZM, respectively, after 24 h of immersion. This rapid change in pH is attributed to the polyacrylic acid and phosphate ions released during the first 24 h of the immersion. Furthermore, the decreasing pH can be correlated to the formation of mineralized bone-like apatite, consuming the alkaline environment (hydroxyl ion uptake) of the immersion SBF solution. The apatite-like structure is formed because of negatively charged Si–OH and COOH groups in the PAC matrix, which have an inductive influence. The addition of PACs in the SBF media increased calcium concentration on reaction with the negatively charged ions, forming a complex attracting phosphate ions, and initial apatite nucleation occurs. The subsequent HCA formation proceeds with the consumption of hydroxyl ions, prompting an increase in H^+ release for equilibration and a related fall in pH of the solution. The higher decrease in pH of the *m*ZM group compared to the Control group could thus be attributed to the higher amount of HCA formation.

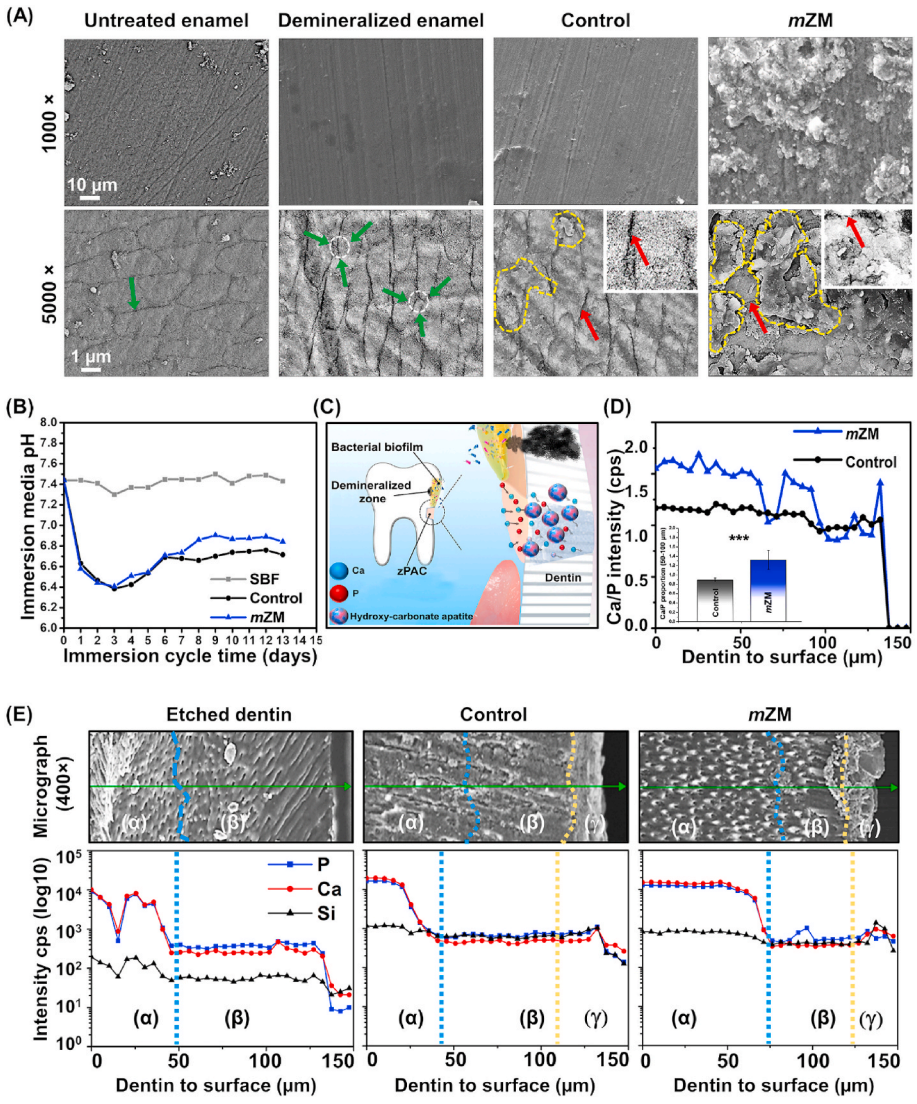

Fig. 5. *Ex vivo* bioactivity assay in dual; passive bovine enamel surface remineralization model and with active bonding to human dentin surface model. (A) SEM micrographs of changes in bovine enamel superficial surface mineralization (Figure S10A) between Control and *m*ZM, with magnifications of 1,000 × and 5,000 × . The green arrows highlight the enamel rod structure with a marked widening of surface interrod spaces characteristic of demineralized zones such as those annotated with dotted circles. At 5000 × , the dotted yellow line marks the region showing active remineralization tendency with deposits of calcium-phosphate-rich compounds aiding in surface remineralization. The red arrows indicate the surface rod structure of the previously widened demineralized surface rod pattern. The insets for Control and *m*ZM show the patent (in Control) and obliterated (in *m*ZM) interrod area acquired at the higher magnification of 20,000 × . The micrographs show a scale bar of 10 μm at 1000 × and 1 μm at 5000 × . (B) Periodic changes in pH of the simulated body fluid (SBF) after 14 days of immersion for bovine enamel surface remineralization acquired at a 24h interval. The Control and *m*ZM group ($n = 6$) were contrasted against as-received pristine SBF solution subjected to identical conditions. (C) Schematic illustration of the ionic diffusion from the cement interface aiding in dentinal remineralization by forming hydroxy-carbonate apatite. The *ex vivo* experiment design is detailed in Figure S10B. (D) Mean intensity changes in the calcium (Ca) and phosphate (P) ratio observed using an energy-dispersive x-ray spectroscopy (EDS) line scan between Control and *m*ZM across the dentinal section. Inset showing the statistically significant differences in Ca/P ratio observed with Mann-Whitney *U* test (n=5, $p < 0.01$). (E) Detailed group-wise results of the *ex vivo* human dentin remineralization experiment expressed as the line scan analysis from the inner sound dentin (α), through demineralized/etched dentin (β), up to the cement (γ) region. The SEM micrographs are paired in a column with the respective line-scan intensity plot for Ca, P, and silica (Si) changes. The length of the green arrow corresponds to the x-axis (150 μm). For both *ex vivo* remineralization experiments $n \geq 5$.

Previous studies have shown that the phosphate concentration of SBF initially increased and then dropped to nearly zero upon depletion with the initial release from glass and formation of apatite [58]. Therefore, it is considered that apatite analogs are formed in the early stage after SBF immersion, and the pH is increased owing to the increase of cations (including Ca and Zn). The ion release profile of the corresponding SBF solutions, following the 14 days of immersion in SBF (Figure S11), showed a higher concentration of cations (Ca, Zn) in the *m*ZM group than Control, validating the rise in pH owing to the reaction of the cations to the protons from the solution [59].

The second experiment of *ex vivo series* (Figure S10B) was performed on an etched dentin surface from extracted human premolars to analyze the dentin remineralization efficacy of the surface-bonded PAC by diffusion of ions stimulating reparative HCA formation (Fig. 5C). EDS-line scan analysis was conducted at the interface of cement-demineralized dentin, and the representative scan plots are documented in Fig. 5D and E. When we compared the ratio of calcium to phosphate (Ca/P) in the length of the line scan (Fig. 5D), a significantly (Fig. 5D inset, $p < 0.001$) higher proportion was observed in *m*ZM (*ca.* 1.3) in comparison to the Control group (*ca.* 0.89) within the 50–100 μm length of the demineralized zone (β). The line scan profile in Fig. 5E provides a detailed comparison between the groups. The *m*ZM group showed a marked difference in the Ca and P intensity profile in the demineralized zone (β) compared to the Control group. The higher intensity was mainly recorded for P in the *m*ZM group, which could be attributed to the upregulation of ion release as an impact of multivalent ZMs. Control and *m*ZM showed Si ions in the deeper layers, notably absent in the untreated etched surface. The Ca/P ratio observed in these results was below the ratio in apatite (Ca/P: 1.67) [60]; however, an exact stoichiometry in biomimetic apatite is not expected. The lower ratio could be attributed to a mixture of octacalcium-phosphate or carbonate substitution in the apatite lattice [61,62].

2.5. Functional therapeutic efficacy of *m*ZM in an intraoral *in vivo* model

Having validated the amplification of bioactivity in the earlier experiments, we planned an *in vivo* experiment using a medium-sized dog model to evaluate the therapeutic efficiency of the zPAC with *m*ZM. An *in vivo* tooth-restoration model was designed to permit simultaneous assessment of bioactivity and multispecies biofilm resistance.

Hypersensitivity of teeth is a debilitating condition widespread in the population, affecting people of all ages. Etiologically, a progressively demineralizing interface at the surface of the exposed dentin (direct/through thin enamel) as a factor of microbial and dietary challenges

leads to chronic pain and discomfort [63]. Recent clinical trials have also considered the evaluation of bioactive glasses as promising candidates to reduce hypersensitivity [64]. The universal applicability of zPAC can permit easy application in coronal and exposed root (deeper periodontal) surfaces. Furthermore, using an *ex vivo* enamel remineralization assay, we observed a tendency for calcium-phosphate-rich precipitates and apatite nucleation permeating into the subjacent dentinal tubules (Figure S12). Thus, for the current oral *in vivo* model, we assessed the bioactive potential of the cement by examining the successful plugging of the superficial dentinal tubules and preservation of the deeper tissue. The intra-oral model comprises a prepared canine surface (box-shaped cavity) in all four quadrants (Fig. 6A), bypassing the superficial enamel layer and filling the PAC on the exposed dentinal floor until flush with the external surface (Fig. 6B and C).

After 14 days, we sectioned and imaged the PAC-dentin interface using SEM (Fig. 6D). The transverse plane micrographs for *m*ZM showed a distinct change in the dentinal microtubules opening with a higher tendency for tertiary dentin formation (Fig. 6D, yellow arrow (left column)). As depicted in the insets, the intratubular network representative of tertiary dentin could be observed in *m*ZM while the Control group had 'clean'-outlined tubular openings. Such reparative behavior could also be confirmed from longitudinal sections (Fig. 6D, blue arrows (middle column)) showing intratubular deposits (*m*ZM > Control) at various depths from the interface with the cement.

As no additional conditioning and artificial demineralization of the dentin was conducted, we also examined the pulp-ward fibrillar structure, otherwise susceptive to non-alkaline pH. These microfibril structures (Fig. 6D, green arrow (right column)), attached to the dentin walls, form a continuous structure in the dentinal tissue associated with the odontoblastic process [65]. Apposite weaved microfibril networks were observed in the *m*ZM specimen in clear contrast to the discontinuous microfibril network in the Control group. The stable and extended pH neutralization capacity (above the critical pH) of the *m*ZM group (Fig. 3B) could have aided in preserving the sensitive network of the microfibrils in the deeper layers.

The remineralization of the predominantly acellular structure of the dental hard tissue i.e., enamel and dentin experiences remineralization via epitaxial deposition of the calcium and phosphate ions [66]. For this reason, the concentration of the calcium and phosphate ions which can be made directly available to the hypomineralized regions is critical to allow healing via remineralization. Therefore, the network modifying action of *m*ZM facilitating a multi-fold increase in ion release increases the drive towards remineralization process for hypomineralized regions in enamel and dentin. The results of the present study largely vindicate the same in both *ex vivo* and *in vivo* assays.

While the *m*Zm action through NBO/BO interaction augments the elution of inducerons for an extended period of time (Fig. 3C and Figure S4), the inherent composition of the glass (*e.g.,* G338 glass commonly use in PACs [7]) dictates the magnitude of inducerons released. Bio-mimetic mineralization composed of cell signaling

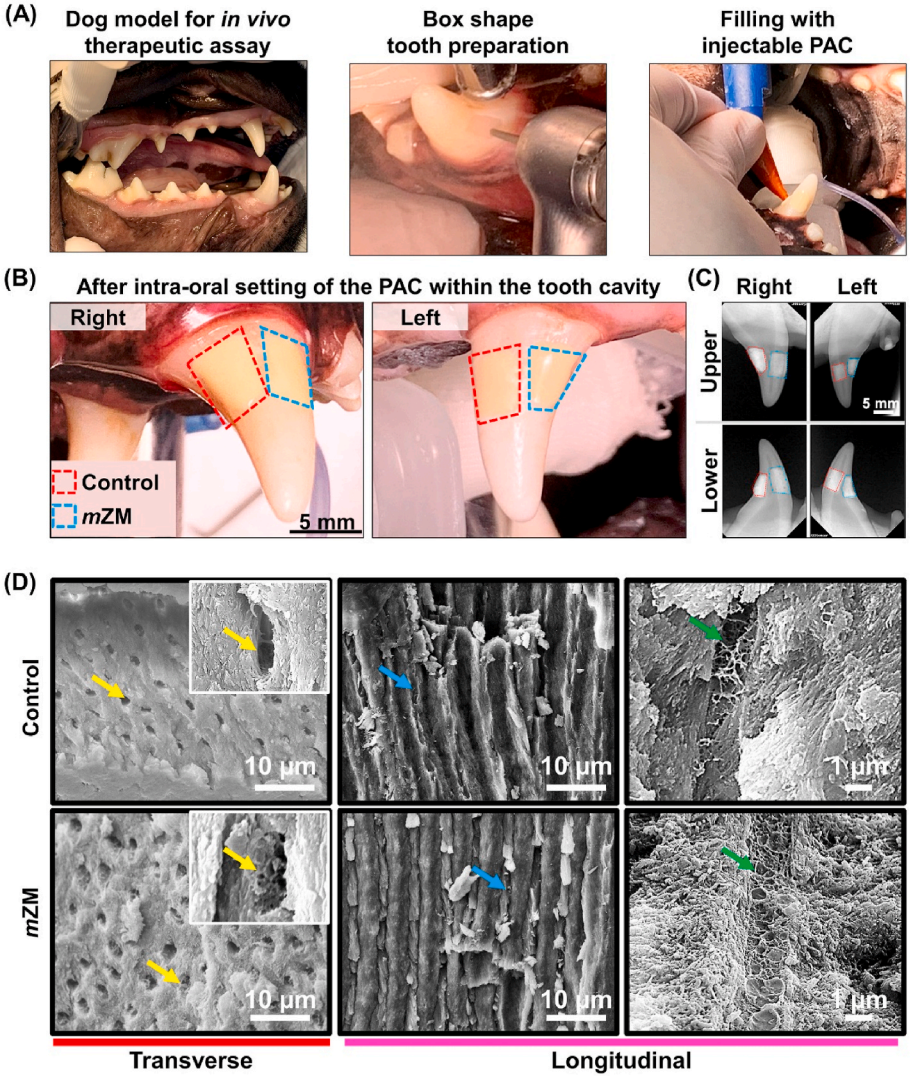

Fig. 6. *In vivo* bioactivity assessments in a medium-size dog model. (A) Intra-oral photographs of the operative procedure, including tooth preparation (box-shape) with a high-speed diamond rotary cutting handpiece and cartridge-based application of PACs over the exposed dentin surface, completed flush with the natural tooth surface. (B) Tooth cavities on the labial surface filled with Control (red dashed box) and *m*ZM (blue dashed box) in various anteroposterior locations on the right and left sides. (C) Post-treatment intraoral periapical radiographs of upper and lower canines in four quadrants characterized by bright radiopacity from the PAC. Scale bar is 5 mm in B and C. (D) SEM micrographs of the region adjacent to dentin-bonded Control and *m*ZM. Transverse plane micrographs (left column at 2,000 ×) contrast the patency of the dentinal microtubules through insets at higher magnification (10,000 ×). The longitudinal section (middle column at 2,000 ×) of the Control and *m*ZM details the extent of the intratubular deposits (blue arrows) at various depths from the cement interface. Representative micrographs (right column at 10,000 ×) showing the microfibril structures (green arrow) within the pulp-ward dentinal tubules attached within the dentin walls. Both Control and *m*ZM were placed on anterior teeth ($n = 4$) per experiment.

pathway has shown a correlation effect to the concentration of the calcium and phosphate, specifically concerning collagen mineralization [67].

Additionally, the concentration of the ions in the cell culture media tends to influence the growth and differentiation of the cells aiding mineralization. Preliminary examination to review the influence of increased ion elution in *m*ZM was examined for cellular (human dental pulp stem cells (hDPSCs)) response in the present study (supplemental methods). The culture media with *m*ZM depicted a thrust in anabolic cell response with improved cell proliferation (Figure S13, $p < 0.01$). The alkaline phosphate activity (Figure S14, $p < 0.05$) and alizarin red assay (Figure S15, $p < 0.01$) also showed a significant increase in *m*ZM compared to Control. The positive effect on cell response reveals a strong plausibility towards biomimetic mineralization. However, to predictably maximize the cellular response, additional optimization of the glass composition and factors influencing the polymerized PAC network (*e.g.,* powder: liquid ratio) would demand further research; and be an important aspect in mineralization targeted cements.

After filling the tooth surface, the PAC (Control and *m*ZM) surface was exposed to the oral environment, allowing simultaneous evaluation of the surface planktonic fouling tendency *via.* taxonomic classification from periodic samples (Figure S16). The microbial community composition analysis from the bio-interactive surface of the PAC displayed a tendency for *m*ZM to favor healthier plaque formation. At all observation time points (days 7, 10, and 14), the rarefied amplicon sequence variant showed a reduction in the average number of observed species when contrasting Control (Fig. 7A, left) with *m*ZM (Fig. 7A, right). As seen in Fig. 7B, diversity indices presented a rich pattern of change in contrast to the evenness of the bacteria species markedly evident on day 7 and day 10. *m*ZM group showing the same richness up to day 10 shows an improvement in the evenness of the distribution. Such a difference could indicate the planktonic environment's dynamism where the transition from primary to secondary colonizers of the biofilm occurs. At day 10, Control showed the same richness; however, the lower evenness indicated a predilection possibly resulting from a selectively conducive niche. The statistical analysis of similarity for the taxa having relative

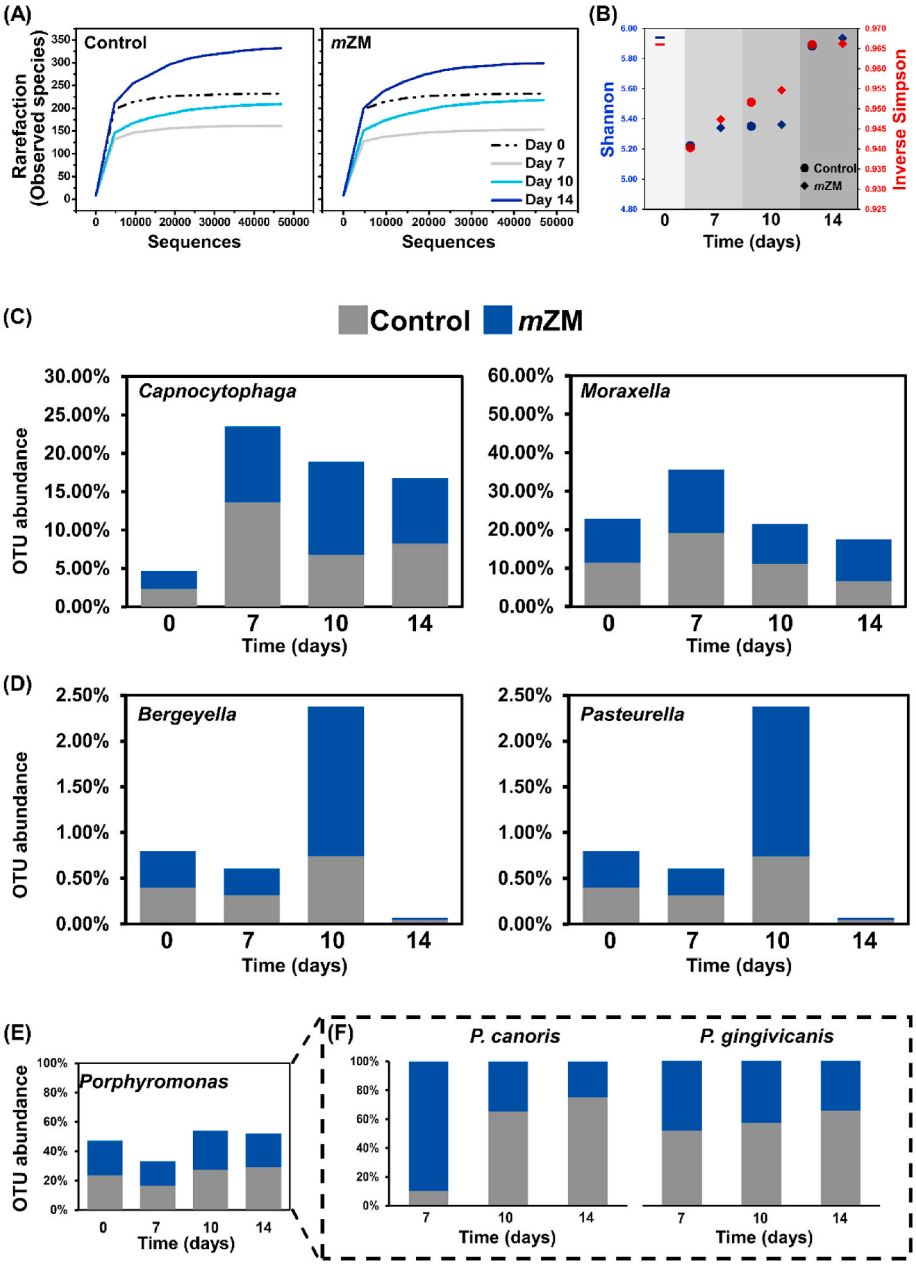

Fig. 7. Analyses of intraoral microbiome at the PAC interface. (A) Rarefaction measure indicates the average number of species observed at different sampling intervals at the same number of sequence cycles. (B) Alpha-diversity indices, Shannon and Inverse Simpson, representative of the bacterial species richness and evenness. (C–D) Comparison of genus-level OTU distribution of the commonly observed and representative taxa. (C) Core microbiota, *Capnocytophaga* sp. (left) and *Moraxella* sp. (right) associated with salivary microbiome of dog. (D) Health-associated bacterial species in the salivary microbiome of dog saliva represented here are *Bergeyella* sp. (left), and *Pasteurella* sp. (right). (E) Distribution of pathogenic *Porphyromonas* sp. between the Control and *m*ZM. (F) Marked increase in relative distribution of specific pathogenic species, *Porphyromonas canoris* (left) and *Porphyromonas gingivicanis* (right), in Control, compared to *m*ZM. Salivary samples were collected in duplicate per stage.

abundance above two percent, resulted a global R value of 0.75 when comparing Control and *m*ZM. We also analyzed the changes in microbial composition as a factor of time and a global R value of 1 with significant differences between the taxa was observed. We performed SIMPER analysis comparing changes within groups from the baseline (day 0, pristine tooth surface) to characterize this further. The Control group presented with a rebound in dissimilarity of composition at day-14 after a mild reduction on day-10 (Figure S17, Tables S8). However, for *m*ZM a progressively reducing average dissimilarity could be observed (Figure S17, Tables S9).

Furthermore, for the documented representative core microbiota (*Capnocytophaga* sp., *Moraxella* sp.) and commensals (*Bergeyella* sp. and *Pasteurella* sp.) from the healthy plaque of dog teeth, a higher favorability for growth was seen in the samples from *m*ZM (Fig. 7C and D) [68]. In contrast, the metabolically flexible and pathogenically dominant *Porphyromonas* sp. were particularly prevalent in the Control group, mainly observed on days 10 and 14 after the application treatment (Fig. 7E). The species-level analysis of the sample revealed the presence of *P. canoris* and *P. gingivicanis*, increasingly dominant in the Control group with progressive biofilm maturation (Fig. 7F). Typically, a unidirectional colonization pattern occurs during the formation of biofilm, such that at the outset, specific bacteria bond and initiate biofilm formation. After the environment is prepared, secondary colonization occurs, resulting in a mixed-species community [69]. The ecological balance between the health-associated (commensal) and the disease-associated (pathogenic) bacteria defines the state of the biofilm and its virulence. Although the bacterial population is widely divergent in the dog plaque compared to the human plaque, from our observations, we could conclude a higher penchant for *m*ZM to support (i) fewer species, (ii) even distribution, and (iii) subsequently, a health-associated community rich plaque. These findings could also be inferred in light of ecological hypothesis of oral disease [70] which suggests that a more balanced biogenic habitat offers resilience to dysbiosis and favors healing and restoration (Figure S18, Supporting note).

3. Conclusion

In summary, the present study presented a method for modifying the polyalkenoate cement network with ZM. Non-zero charged *m*ZM effectively changed the BO network, which increased NBO proportion. Cytocompatible *m*ZM showed an upregulation of ion release with augmentation of NBO-induced ion channels. The improved ionic interaction displayed an efficient pH neutralization, which yielded an environment for enhancing bioactivity. Improvement of bioactive potential was seen as a noticeable increase in HCA formation ability. The diffusion of ions across the hard-tissue interface led to effective remineralization *ex vivo* and *in vivo*. The ZM also imparted efficient bacterial biofilm resistance arising under the harmonious influence of divalent cations. The *m*ZM effect in zPAC led to a shift in the multispecies bacterial biofilm, reducing *ca.* 68% biofilm mass compared to Control. Overall, the surface biofilm in contact with *m*ZM presented a preference for a 'healthy' balanced microcosm environment. The results indicated that combining multivalent zwitterionic modifiers with good bioactivity and excellent biofilm resistance can be adapted for targeted therapeutic applications. The findings from our study exploring the original concept and application of zwitterionic derivatives towards ionic upregulation is also prospective of *m*ZM to upregulate the osteoinductive properties. Adapting the discussed network modifying effect in PAC-type bioactive cements holds promise for biomimetic mineralization, though an in-depth understanding of cellular responses will call for further research.

Therefore, the augmentation of induceron elution by the action of the modifiers has the potential to be expanded in the development of cement-like adhesives with tailored compositions favoring site-specific tissue regeneration.

4. Materials and methods

4.1. Preparation of zwitterion-incorporated polyalkenoate cement

A powder-liquid type glass polyalkenoate cement (PAC) composed of fluoroaluminosilicate and fluorozincsilicate glass parts (Caredyne Restore; GC Corporation, Tokyo, Japan) was used as a Control in this study [37]. Two zwitterionic derivatives-2-methacryloyloxyethyl phosphorylcholine (MPC; Sigma-Aldrich, St. Louis, MO, USA) and sulfobetaine methacrylate (SBMA; Sigma-Aldrich, St. Louis, MO, USA), were used for experimental groups. The liquid was homogenized with 3% mass fraction of zwitterionic derivatives adapting the protocol optimized elsewhere [20]. The combinatorial *m*ZM comprised both derivatives while unitary zwitterionic system included MPC alone and formed the *s*ZM.

4.2. Structural characterizations of PAC

TGA (TGA 4000, PerkinElmer, Korea) was exploited to interpret the structural decomposition based on the mass reductions. The average mass of initial PACs was about 17.5 mg, and the heating rate kept as 10 °C/min until 800 °C. XPS (K-ALPHA, Thermo Fisher Scientific, USA) and Raman spectroscopy (XploRA™ PLUS, HORIBA, France) were performed to investigate the bridging oxygen/non-bridging oxygen (BO/NBO) structures of zPACs. The 10 × microscope objective (numerical aperture = 0.25). The 532 nm laser was exposed for 30 s. The confocal diameter was 100 μm. The grafting was set as 1800 grating. The laser intensity was *ca.* 75 mW, and spatial laser spot size was 2.6 μm (diameter). 520 cm^{-1} peak of the silicon was the calibration peak before the measurement. In order to get reliable data, we repeated the measurements five times.

The thermal characterization, such as dehydration and decomposition of the PACs was determined using differential scanning calorimetry (DSC 404F3, Netzsch, Germany). The heat flow between a PAC sample and the reference was measured by power compensation. The samples were heated in the temperature range from 30 °C to 800 °C with a heating rate of 10 °C/min under an argon gas flow. The sample weight was 15–20 mg. Further, the hydration ability was measured by Raman spectroscopy following the procedure in previous studies [21,22]. Briefly, prefabricated PACs were fully hydrated in DW for 6 h prior to the Raman measurements. Then, the bulk water was removed by slightly tilting the substrate. The detailed experimental condition was consistent to the protocol [4,5].

4.3. In vitro ion release profile of PACs

In the experiment to analyze the elution of ions, a disc-shaped specimen with a diameter of 10 mm and a height of 2 mm size was used (n=3). The specimen was immersed in 5 mL of distilled water and stored at 37 °C for 24 h. After the incubation, elemental analysis of the zinc, sodium, calcium, strontium, aluminum, silica and phosphate ion release profiles were obtained by inductively coupled plasma optical emission spectrometer (ICP-OES, Agilent 5100, Agilent Technologies, CA, USA). We also quantitatively evaluated fluoride ion release using fluoride specific electrodes (920A, Orion, Boston, USA).

4.4. Long term elution of inducerons from PACs

Pellets of each PAC cement (Control, *s*ZM and *m*ZM) were prepared as described above, measuring 10 mm in diameter and approximately 2 mm in height. Three pellets of each PAC group were then submerged in 5 cm^3 of distilled water (pH = 5.57). With this volume of water, all pellets could be completely submerged in a 15 cm^3 conical tube. The tubes were sealed and incubated at 37 °C, in adherence to an earlier protocol [71]. To assess the cumulative ion release, the elute media was collected progressively at different time points (1, 3, 7, 14, 21 days) and

the solution was regularly refreshed [40]. The elution was stored at 37 °C in sealed tubes prior to elemental analysis using an inductively coupled plasma optical emission spectrometer (ICP-OES, Agilent 5100, Agilent Technologies, CA, USA). Data was analyzed from a minimum of three replicate samples for each group.

4.5. In vitro pH neutralization by PAC

Acid neutralization capacity was analyzed by studying the dynamic pH change of lactic acid. The size of the specimen used to observe the pH neutralization was 2 × 2 × 25 mm. Lactic acid (Sigma-Aldrich, Steinheim, Germany) was diluted in distilled water to a pH of 4.0 and three specimens were immersed into the buffered lactic acid solution (2.14 mL). The volume ratio of the specimen and the solution was matched at 0.14:1 as per the previous study [72]. Changes were detected in real time using a digital pH meter (Orion 4 Star, Thermo Fisher Scientific Inc., Singapore). pH data was collected per min up to 400 min.

4.6. In vitro bioactivity assay of PACs

The apatite forming ability was investigated by depicting apatite formation on the zwitterion-incorporated PAC discs in the presence of a simulated body fluid (SBF, Table S6) [73]. The zPAC discs were prepared with a diameter of 15 mm and a height of 2 mm. The morphology, quantification, and chemical changes of the deposited layer on the surface of zPAC discs were assessed after immersion in SBF (5 mL) after 1 day and 7 days. The morphology and quantification (percentage ratio) of the precipitated layer were determined using a field-emission scanning electron microscope (FE-SEM, JSM-7800 F, JEOL, Akishima, Tokyo, Japan) and ImageJ software (NIH, Bethesda, MA, USA).

4.7. In vitro analysis specie specific bacterial resistance

Sterptococcus mutans (KCOM 3478) and *Staphylococcus aureus* (KCOM 1491) were selected as the representative species to evaluate the bacterial resistance the PAC as a factor of ZMs. The representative bacteria were separately added to 2% sucrose Brain Heart Infusion (BHI) broth media and incubated at 37 °C for 18 h or longer under aerobic environment. The optical density (OD_{600}) was adjusted (*S.mutans*: 0.05; *S. aureus*: 0.3) and the diluted bacterial suspension was directly inoculated over the disc shape samples (n=6).

After aerobic incubation at 37 °C for 24 h analysis of colony forming units (CFU) and live/dead bacteria assay was performed. For CFU estimation (n=3), sonication was performed for 5 min to separate the attached bacteria from the specimen [20]. Only the isolated bacteria were diluted with distilled water and spread on BHI agar. After 24h culture on the agar plates, CFU was calculated by counting the number of colonies that appeared on the BHI agar and plotted factoring the dilution. For live/dead bacteria analysis (n=3) of the attached single-species biofilm, a mixture of SYTO 9 (2.5 μM) and propidium iodide (2.5 μM) (Live/Dead Baclight Bacterial Viability Kit) was used to stain the samples. The stained images were visualized using confocal laser scanning microscopy (CLSM, LSM880, Carl Zeiss, Thornwood, NY, USA).

In addition, after removing the specimen from the bacterial solution inoculated with bacteria, the remaining bacterial suspension was pipetted, and 100 μL was seeded in a 96-well plate to measure the OD_{600} using a microplate reader (Epoch, BioTek Instruments, VT, USA). The OD values relative to the untreated bacterial suspension-cultured parallel to the experimental groups was also recorded for both representative bacteria.

4.8. Ex vivo multispecies human salivary biofouling resistance

Biofilm analysis was conducted using a mixed collection of six individual human saliva, following approval from the ethics committee (IRB No. 2-2019-0049). Specimens manufactured in a size of 5 × 1.5 mm were used. McBain broth media and saliva collection were mixed in a ratio of 50:1 and dispensed into each specimen containing well (1.5 mL). The McBain broth is media supplemented with mucin (type II, porcine, gastric) (2.5 g L^{-1}), tryptone (2.0 g L^{-1}), bacteriological peptone (2.0 g L^{-1}), yeast extract (1.0 g L^{-1}), NaCl (0.35 g L^{-1}), $CaCl_2$ (0.2 g L^{-1}), KCl (0.2 g L^{-1}), cysteine hydrochloride (0.1 g L^{-1}), haemin (0.001 g L^{-1}), and vitamin K1 (0.0002 g L^{-1}). Maintained at 37 °C in a 5% CO_2 incubator, the McBain broth was changed after 8 and 16 h [22]. After the last replacement, mixed saliva was 24 h further incubated. After removing the specimen from the suspension, it was gently rinsed twice in distilled water to remove non-adherent microorganisms. Using a live/dead bacterial viability kit (Molecular Probes, Eugene, OR, USA), the dead microorganisms were stained red and the living microorganisms green. Images were captured using confocal laser scanning microscopy (CLSM, LSM980, Carl Zeiss, Thornwood, NY, USA). Biothickness was calculated using Zen (Zen, Carl Zeiss, Thornwood, NY, USA) software. The COMSTAT plug-in (Technical University of Denmark, Kongens Lyngby, Denmark) in ImageJ (NIH, Bethesda, MA, USA) was used to determine the average biomass [74].

4.9. DNA sequencing of human salivary oral biofilm

DNA sequencing was performed to identify the biofilm composition on the PAC specimens with and without the ZMs. Mixed saliva of six healthy adults was cultured on the specimen using the method described in the previous section. According to the manufacturer's protocol, the bacterial DNA obtained from the specimen was extracted using DNeasy PowerSoil Kit (Cat. No. 12888–100, QIAGEN). Each sequenced sample was prepared according to the Illumina 16S Metagenomic Sequencing Library protocols. The quantification and quality of DNA was assessed by PicoGreen (Promega) using VICTOR Nivo (PerkinElmer). The 16S rRNA genes were amplified using 16S V3–V4 primers. Input gDNA was amplified with 16S V3–V4 primers, and a subsequent limited-cycle amplification step was performed to add multiplexing indices and Illumina sequencing adapters. The final products were normalized and pooled using the PicoGreen. The size of libraries was verified using the TapeStation DNA screentape D1000 (Agilent), followed by sequencing with the MiSeq™ platform (Illumina, San Diego, USA).

4.10. Ex vivo remineralization analysis

The *ex vivo* remineralization efficacy evaluation was conducted in a simulated demineralization treatment for enamel and dentin as two separate experiment setups (Figure S10). For enamel remineralization, bovine incisors were used, while the effect of direct cement bonding to dentin was evaluated on the extracted human teeth [55].

Freshly extracted bovine teeth were used to prepare the enamel slabs to compare the surface remineralization between the Control and *m*ZM. The bovine incisors were embedded in epoxy resin while leaving the labial surface exposed, followed by storage in distilled water to eliminate residual monomer. After 48h, specimens were polished with sandpapers using grit of #800, 1200, and 2000 consecutively. The polished specimens were ultrasonicated for 10 min in an ultrasonic cleaner to eliminate the smear layer. A sub-surface demineralized carious lesion was developed ahead using a dynamic acidic environment. In brief, the samples were immersed in lactic acid (pH = 4) for 72 h in a shaking incubator (37 °C, 50 rpm) without solution refreshing. The demineralized samples were sterilized by ethylene oxide before bacterial biofilm culture.

For the bacterial biofilm treatment, *S. mutans* (KCOM 3478) was cultured overnight at 37 °C in BHI broth. The suspension was adjusted to an optical density (OD) of 0.5 at 600 nm by dilution with BHI. The sterilized enamel slabs were then placed into the 12-well plates and with the exposed labial surface facing up and immersed in 2-mL of the adjusted bacterial suspension. The plates were incubated at 37 °C for 24

h to simulate the cariogenic challenge by the *S. mutans* biofilm. Before start of the remineralization cycle, the demineralized enamel slabs (under simulated *S. mutans* cariogenic treatment) were rinsed in the ultrasonic bath with distilled water for 30 min followed by air drying. The ultrasonic rinsing in DW ensures stoppage of the demineralization cycle before interaction with the remineralizing PAC [55].

The prefabricated Control and *m*ZM PAC pellets, were sterilized with ethylene oxide for further use. The now rinsed enamel specimens (n=5) were approximated with the cement pellets (Control and *m*ZM) and immersed in SBF. Each immersion environment was matched according to the results of the ion release profile, with PAC having a cement to volume ratio of 0.09/1. Complete submersion of all enamel slabs approximated with PAC pellets was ensured by placement in 50 cm^3 conical tubes. In addition to experiment groups, a sample each of untreated enamel and surface demineralized enamel was also immersed in SBF alone. Hence, twelve specimen-immersion tubes were prepared, sealed, and stored in constant relative humidity at 37 °C for 14 days.

For all the tubes, static analysis of the change in immersion media pH was conducted at a 24 h interval with a digital pH meter (Orion 4 Star, Thermo Fisher Scientific Inc., Singapore), calibrated at pH 4.01, pH 7.00 and pH 10.01 immediately before use.

After 14 days of remineralization treatment in SBF, cement specimens were removed, and enamel samples were rinsed in distilled water and dried before scanning electron microscopy (SEM) examination. The superficial surfaces (exposed surfaces) were sputter-coated with gold (300 Å) and examined *via.* SEM (JEOL-7610F-plus microscope, Tokyo, Japan). The SBF solution obtained after 14-day immersion was also evaluated for ion release profiles for Si, Ca, P, S, Zn and Al, and compared against the same for the SBF stored at 37 °C.

For *ex vivo* analysis of the human dentin remineralization by direct cementation, randomly collected sound premolars from the human oral cavity (gathered as approved by the institutional review board of the Yonsei University Dental Hospital (Seoul, Republic of Korea; 2-2019-0034). The teeth were cut in slices of 2–3 mm thickness at the middle and cervical third level using a low-speed precision diamond saw (DAIMO-100S; MTDI, Daejon, Republic of Korea) and polished with 1000,1200 and 2000-grit SiC papers. The cut sections were then ultrasonicated in distilled water to remove the smear layer. The dentin surface was verified for the absence of enamel and/or pulp tissue under a stereomicroscope at 100 × . The exposed dentin surfaces were demineralized using a 17% ethylene diamine tetraacetic acid (EDTA) solution (MD-Cleanser™, Meta Biomed Co. Ltd., Cheongju City, Chungbuk, Korea) for 6 h. After demineralizing, teeth were rinsed in the ultrasonic bath with distilled water for 30 min. The Control and *m*ZM PAC were mixed and placed directly onto the etched dentin surfaces under magnification with a cartridge-type dispenser. The cement was placed such that no more than half of the surface was covered with cement (n=5 per group). Each tooth was immediately immersed in SBF solution (10 mL) in a 6-well plate and stored at 37 °C in constant humidity for 14 days.

After storage, the teeth were embedded in epoxy resin, and cross-sectioned perpendicular to the surface utilizing a water-cooled diamond saw for SEM/EDX examination of the cement-dentin interface.

In preparation for SEM/EDX, the treated samples were desiccated using critical point drying (LEICA EM CPD300; Leica, Wien, Austria). The samples were then mounted on stubs and vacuum sputter-coated with carbon to reduce electrostatic charging. All the treated models prepared for the SEM (Merin, Carl Zeiss, Oberkochen, Germany), equipped with a QUANTAX 200 detector (Bruker GmbH, Berlin, Germany) at 12 kV for EDX analysis. The EDX measurement used a spot size of 0.75 μm. The measurements were performed on the surface of the cross-sections, starting at the inner layer normal dentin, and moving outwards to the treated/untreated surface [75,76]. In total, 60 measurements were taken at every 5 μm distance per line scan from the dentin to outer cement surface. The content of phosphate (P), calcium (Ca), and silica (Si) was analyzed at each measurement point.

4.11. Therapeutic efficacy of mZM in an in vivo animal model

Animals: Two healthy male mongrel dogs, 10–14 months of age and weighing approximately 25–30 kg, were included in this study in compliance with the ARRIVE guidelines, approved by the Yonsei University Health System Institutional Animal Care and Use Committee, Seoul, Republic of Korea (Approval No. 2019–0068). The animals were housed and monitored daily for the study duration in the Department of Laboratory Animal Resources, Yonsei Biomedical Research Institute, Seoul, Republic of Korea. They were allowed a week for acclimation prior to the experiment. They were kept in individual cages at 22 °C with a relative humidity of 50% and a 12-h light/dark cycle. Approximately 500g of solid food (Purina; Nestle SA, Vevey, Switzerland) was provided to each animal every day, and water was available ad libitum during the experimental period.

Intervention: Canine teeth of all four quadrants (teeth 104, 204, 304, 404) of each animal were included in the experiment. An experienced dental clinician performed all procedures under general and local anesthesia under aseptic routines. General anesthesia was induced by alfaxalone (Alfaxan; Jurox Pty Ltd., Rutherford, NSW, Australia), medetomidine hydrochloride (Tomidine; Provet Ltd., Istanbul, Turkey) intravenously and was maintained by 2% isoflurane (Ifran Liq; Hana Pharm Co Ltd., Republic of Korea) in conjunction with pure oxygen by inhalation.

Two box-shaped cavities were prepared on the cervical third of the labial surface of all canines using a sterile diamond bur with a high-speed dental handpiece. All tooth preparation was of a minimum depth of 2 mm with a smoothened cavity base at the dentin level. The PACs were applied with injectable cartridges (Compules Tips, Dentsply Sirona) to fill the cavities directly. On the left side (teeth 204 and 304), the prepared anterior and posterior cavities were restored with Control and *m*ZM, respectively, and vice-versa on the right side (teeth 104–404).

Microbiome sequencing and ecological indexing: The plaque swabs were collected before the intervention and at days 7, 10, and 14 after the PAC application, using a sterile 1 μL plastic loop and collected into a 1 mL micro-centrifuge (Figure S16). Before the cavity preparation, the plaque was collected from the outer labial surfaces of the four canine teeth (teeth 104, 204, 304, and 404) and pooled (day 0). Additionally, plaque samples were collected from the surface of the cavities restored with the Control and *m*ZM group on days 7, 10, and 14 after the restorative treatment and pooled separately. Regular feeding schedules was maintained for the *in vivo* experiment to otherwise eliminate dietary factor as a change. Taking into account the repeatability and quality control in the sampling protocol, the sampling periods were scheduled such that a minimum of 12 h from the last meal, with absence of any additional oral-prophylaxis measures through the period of assessment. The collected specimens were filtered to remove the bacteria and stored for sequence processing and analysis. The processing was similar to as described in *ex vivo* analysis. Metagenome amplicon sequencing and 16S rRNA of V3 to V4 were analyzed using Bakt 41F-805R target region. The best BLAST hit in the COMD database (version NCBI_16S_20210518) was chosen as the reference for each representative sequence.

Additionally, periapical radiographs were taken on the day of restoration, before and after restorative tooth treatment, and weekly intervals. After the surgical procedures, the animals were administered ketorolac tromethamine (Keromin inj; Hana Pharma Co Ltd., Republic of Korea), Cefazolin sodium (30 mg/kg, Chonkundang, Republic of Korea), Meloxicam (0.2 mg/kg, Boehringer Ingelheim, Greece) for a week.

Mineralization efficacy PAC at the dentin interface: After 14-day of application of the PAC, all four canines were coronally resected en-block under general anesthesia, and collect specimen were processed for SEM imaging. Briefly, the teeth were fixed in buffered paraformaldehyde. After 48h of fixation, the teeth were rinsed with phosphate-buffered saline (PBS) for 1 h with three changes. Following a 1 min wash with distilled water, the specimens were dehydrated in sequentially concentrated ethanol (25%, 50%, 75%, 95% and 100%)

and immersed in hexamethyldisilazane (Sigma-Aldrich) for 10 min.

The specimens were subsequently embedded in epoxy resin, and sections were cut using alow-speed diamond wheel on a Metsaw (RB205 Metsaw-LS TM; R&B, Daejeon, Korea), which was set at 300 rpm. The sections were made perpendicular to the long axis of the crowns with the thickness of ≈ 2 mm. The sectioned discs were examined perpendicular to the cutting plane and *via.* a secondary perpendicular section through FE-SEM (JEOL-7800, Tokyo, Japan).

4.12. Statistical analysis

The statistical significance was analyzed using One-way analyses of variance (ANOVA). Tukey's multiple comparison test was used to compare the means of each of the groups at a p value of 0.05. For comparison between two groups, Control and *m*ZM in *ex vivo* and cell activity analysis were performed either T-test or Mann-Whitney *U* test. Paleontological Statistics Software (PAST) (Version 4.07 for Windows) [77] and R studio (Version 1.4.1103) statistical platforms were used for analysis of data from genomic sequencing of microbiota. Analysis of similarity (ANOSIM) tests were performed based on Bray-Curtis dissimilarity index [78] to evaluate changes in microbiome composition across time periods *in vivo.* Similarity percentage analysis (SIMPER) was performed to provide information on significant differences between time points and to identify the contributing taxa for the observed differences.

Declaration of competing interest

The authors declare that they have no known competing financial interests or personal relationships that could have appeared to influence the work reported in this paper.

CRediT authorship contribution statement

Ji-Yeong Kim: Methodology, Visualization, Formal analysis, Investigation. **Woojin Choi:** Methodology, Visualization, Formal analysis, Investigation. **Utkarsh Mangal:** Data curation, Writing – original draft, Visualization, Formal analysis, Writing – review & editing, Investigation. **Ji-Young Seo:** Formal analysis, Investigation, Methodology. **Tae-Yun Kang:** Formal analysis, Investigation, Methodology. **Joohee Lee:** Formal analysis, Investigation, Methodology. **Taeho Kim:** Formal analysis, Investigation, Methodology. **Jung-Yul Cha:** Supervision, Resources. **Kee-Joon Lee:** Supervision, Resources. **Kwang-Mahn Kim:** Supervision, Resources. **Jin-Man Kim:** Resources, Methodology, Investigation. **Dohyun Kim:** Resources, Methodology, Investigation. **Jae-Sung Kwon:** Conceptualization, Methodology, Validation, Writing – review & editing. **Jinkee Hong:** Conceptualization, Methodology, Validation, Project administration, Writing – review & editing, Funding acquisition. **Sung-Hwan Choi:** Conceptualization, Methodology, Validation, Project administration, Writing – review & editing, Funding acquisition.

Acknowledgments

This work was supported by the Korea Medical Device Development Fund grant funded by the Korea government (the Ministry of Science and ICT, the Ministry of Trade, Industry and Energy, the Ministry of Health and Welfare, the Ministry of Food and Drug Safety) (Project Number: KMDF_PR_20200901_0067–01), by the National Research Foundation of Korea(NRF) grant funded by the Korea government (MSIT) (No. 2021R1A2C2091260), and by faculty research grant of Yonsei University College of Dentistry (6-2021-0037).

Appendix A. Supplementary data

Supplementary data to this article can be found online at https://doi.org/10.1016/j.bioactmat.2021.11.020.

References

[1] A.K. Gaharwar, S.M. Mihaila, A. Swami, A. Patel, S. Sant, R.L. Reis, A.P. Marques, M.E. Gomes, A. Khademhosseini, Bioactive silicate nanoplatelets for osteogenic differentiation of human mesenchymal stem cells, Adv. Mater. 25 (24) (2013) 3329–3336.
[2] E. Gentleman, R.J. Swain, N.D. Evans, S. Boonrungsiman, G. Jell, M.D. Ball, T.A. V. Shean, M.L. Oyen, A. Porter, M.M. Stevens, Comparative materials differences revealed in engineered bone as a function of cell-specific differentiation, Nat. Mater. 8 (9) (2009) 763–770.
[3] A. Khademhosseini, R. Langer, J. Borenstein, J.P. Vacanti, Microscale technologies for tissue engineering and biology, Proc. Natl. Acad. Sci. U.S.A. 103 (8) (2006) 2480–2487.
[4] J.R. Jones, Review of bioactive glass: from Hench to hybrids, Acta Biomater. 9 (1) (2013) 4457–4486.
[5] L.L. Hench, I.D. Xynos, J.M. Polak, Bioactive glasses for in situ tissue regeneration, J. Biomater. Sci. Polym. Ed. 15 (4) (2004) 543–562.
[6] H. Forss, Release of fluoride and other elements from light-cured glass ionomers in neutral and acidic conditions, J. Dent. Res. 72 (8) (1993) 1257–1262.
[7] K.V. Tian, B. Yang, Y. Yue, D.T. Bowron, J. Mayers, R.S. Donnan, C. Dobo-Nagy, J. W. Nicholson, D.C. Fang, A.L. Greer, G.A. Chass, G.N. Greaves, Atomic and vibrational origins of mechanical toughness in bioactive cement during setting, Nat. Commun. 6 (1) (2015) 8631.
[8] I.M. Brook, P.V. Hatton, Glass-ionomers: bioactive implant materials, Biomaterials 19 (6) (1998) 565–571.
[9] P.V. Hatton, V.R. Kearns, I.M. Brook, Bone–cement fixation: glass–ionomer cements, in: Joint Replacement Technology, 2008, pp. 252–263.
[10] M.C. Blades, D.P. Moore, P.A. Revell, R. Hill, In vivo skeletal response and biomechanical assessment of two novel polyalkenoate cements following femoral implantation in the female New Zealand White rabbit, J. Mater. Sci. Mater. Med. 9 (12) (1998) 701–706.
[11] K.K. Johal, G. Mendoza-Suarez, J.I. Escalante-Garcia, R.G. Hill, I.M. Brook, In vivo response of strontium and zinc-based ionomeric cement implants in bone, J. Mater. Sci. Mater. Med. 13 (4) (2002) 375–379.
[12] C.A. Shaw, L. Tomljenovic, Aluminum in the central nervous system (CNS): toxicity in humans and animals, vaccine adjuvants, and autoimmunity, Immunol. Res. 56 (2–3) (2013) 304–316.
[13] F.O. Gomes, R.A. Pires, R.L. Reis, Aluminum-free glass-ionomer bone cements with enhanced bioactivity and biodegradability, Mater. Sci. Eng. C Mater. Biol. Appl. 33 (3) (2013) 1361–1370.
[14] J.W. Nicholson, Chemistry of glass-ionomer cements: a review, Biomaterials 19 (6) (1998) 485–494.
[15] A. Bernasconi, M. Dapiaggi, A. Pavese, G. Agostini, M. Bernasconi, D.T. Bowron, Modeling the structure of complex aluminosilicate glasses: the effect of zinc addition, J. Phys. Chem. B 120 (9) (2016) 2526–2537.
[16] W.H. Bowen, R.A. Burne, H. Wu, H. Koo, Oral biofilms: pathogens, matrix, and polymicrobial interactions in microenvironments, Trends Microbiol. 26 (3) (2018) 229–242.
[17] P. Ducheyne, Bioactive ceramics: the effect of surface reactivity on bone formation and bone cell function, Biomaterials 20 (23–24) (1999) 2287–2303.
[18] J. Kreth, J.L. Ferracane, C.S. Pfeifer, S. Khajotia, J. Merritt, At the interface of materials and microbiology: a call for the development of standardized approaches to assay biomaterial-biofilm interactions, J. Dent. Res. 98 (8) (2019) 850–852.
[19] J.S. Kwon, M.J. Lee, J.Y. Kim, D. Kim, J.H. Ryu, S. Jang, K.M. Kim, C.J. Hwang, S. H. Choi, Novel anti-biofouling bioactive calcium silicate-based cement containing 2-methacryloyloxyethyl phosphorylcholine, PLoS One 14 (1) (2019), e0211007.
[20] M.J. Lee, J.S. Kwon, J.Y. Kim, J.H. Ryu, J.Y. Seo, S. Jang, K.M. Kim, C.J. Hwang, S. H. Choi, Bioactive resin-based composite with surface pre-reacted glass-ionomer filler and zwitterionic material to prevent the formation of multi-species biofilm, Dent. Mater. 35 (9) (2019) 1331–1341.
[21] W. Choi, J. Jin, S. Park, J.Y. Kim, M.J. Lee, H. Sun, J.S. Kwon, H. Lee, S.H. Choi, J. Hong, Quantitative interpretation of hydration dynamics enabled the fabrication of a zwitterionic antifouling surface, Acs Appl Mater Inter 12 (7) (2020) 7951–7965.
[22] W. Choi, S. Park, J.S. Kwon, E.Y. Jang, J.Y. Kim, J. Heo, Y. Hwang, B.S. Kim, J. H. Moon, S. Jung, S.H. Choi, H. Lee, H.W. Ahn, J. Hong, Reverse actuation of polyelectrolyte effect for in vivo antifouling, ACS Nano (2021).
[23] J.S. Kwon, J.Y. Kim, U. Mangal, J.Y. Seo, M.J. Lee, J. Jin, J.H. Yu, S.H. Choi, Durable oral biofilm resistance of 3D-printed dental base polymers containing zwitterionic materials, Int. J. Mol. Sci. 22 (1) (2021).
[24] D. Arcos, D.C. Greenspan, M. Vallet-Regí, Influence of the stabilization temperature on textural and structural features and ion release in SiO2−CaO−P2O5Sol−Gel glasses, Chem. Mater. 14 (4) (2002) 1515–1522.
[25] D.-S. Guo, K. Wang, Y.-X. Wang, Y. Liu, Cholinesterase-responsive supramolecular vesicle, J. Am. Chem. Soc. 134 (24) (2012) 10244–10250.
[26] C. Fong, T. Le, C.J. Drummond, Lyotropic liquid crystal engineering–ordered nanostructured small molecule amphiphile self-assembly materials by design, Chem. Soc. Rev. 41 (3) (2012) 1297–1322.
[27] T.M. McCoy, A. Valiakhmetova, M.J. Pottage, C.J. Garvey, L.d. Campo, C. Rehm, D. A. Kuryashov, R.F. Tabor, Structural evolution of wormlike micellar fluids formed by erucyl amidopropyl betaine with oil, salts, and surfactants, Langmuir 32 (47) (2016) 12423–12433.

[28] A. Wu, Y. Gao, L. Zheng, Zwitterionic amphiphiles: their aggregation behavior and applications, Green Chem. 21 (16) (2019) 4290–4312.
[29] Q. Shao, S. Jiang, Molecular understanding and design of zwitterionic materials, Adv. Mater. 27 (1) (2015) 15–26.
[30] S.J. Cox, D.G. Thorpe, P.R. Shaffer, P.L. Geissler, Assessing long-range contributions to the charge asymmetry of ion adsorption at the air–water interface, Chem. Sci. 11 (43) (2020) 11791–11800.
[31] T. Wu, F.L. Beyer, R.H. Brown, R.B. Moore, T.E. Long, Influence of zwitterions on thermomechanical properties and morphology of acrylic copolymers: implications for electroactive applications, Macromolecules 44 (20) (2011) 8056–8063.
[32] K. Singh, A. Raghav, P.K. Jha, S. Satapathi, Effect of size and charge asymmetry on aggregation kinetics of oppositely charged nanoparticles, Sci. Rep. 9 (1) (2019) 3762.
[33] S.K. Khalil, E.D. Atkins, Investigation of glass-ionomer cements using differential scanning calorimetry, J. Mater. Sci. Mater. Med. 9 (9) (1998) 529–533.
[34] S. Garoushi, J. He, J. Obradovic, P. Fardim, P.K. Vallittu, L. Lassila, Incorporation of cellulose fiber in glass ionomer cement, Eur. J. Oral Sci. 128 (1) (2020) 81–88.
[35] M.F. Hochella, A.H. Carim, A reassessment of electron escape depths in silicon and thermally grown silicon dioxide thin films, Surf. Sci. 197 (3) (1988) L260–L268.
[36] A.D. Wilson, A hard decade's work: steps in the invention of the glass-ionomer cement, J. Dent. Res. 75 (10) (1996) 1723–1727.
[37] T. Kohno, Y. Liu, R. Tsuboi, H. Kitagawa, S. Imazato, Evaluation of ion release and the recharge ability of glass-ionomer cement containing BioUnion filler using an in vitro saliva-drop setting assembly, Dent. Mater. 37 (5) (2021) 882–893.
[38] Z. Nescakova, K. Zheng, L. Liverani, Q. Nawaz, D. Galuskova, H. Kankova, M. Michalek, D. Galusek, A.R. Boccaccini, Multifunctional zinc ion doped sol - gel derived mesoporous bioactive glass nanoparticles for biomedical applications, Bioact. Mater. 4 (2019) 312–321.
[39] P.Y. Mengsteab, T. Otsuka, A. Mcclinton, N.S. Shemshaki, S. Shah, H.-M. Kan, E. Obopilwe, A.T. Vella, L.S. Nair, C.T. Laurencin, Mechanically superior matrices promote osteointegration and regeneration of anterior cruciate ligament tissue in rabbits, Proc. Natl. Acad. Sci. Unit. States Am. 117 (46) (2020) 28655–28666.
[40] J.W. Nicholson, N.J. Coleman, S.K. Sidhu, Kinetics of ion release from a conventional glass-ionomer cement, J. Mater. Sci. Mater. Med. 32 (4) (2021) 30.
[41] T. Kokubo, Bioactive glass ceramics: properties and applications, Biomaterials 12 (2) (1991) 155–163.
[42] H.-C. Flemming, T.R. Neu, D.J. Wozniak, The EPS matrix: the "house of biofilm cells", J. Bacteriol. 189 (22) (2007) 7945–7947.
[43] E.L. Steiger, J.R. Muelli, O. Braissant, T. Waltimo, M. Astasov-Frauenhoffer, Effect of divalent ions on cariogenic biofilm formation, BMC Microbiol. 20 (1) (2020) 287.
[44] Y. Shen, P.C. Huang, C. Huang, P. Sun, G.L. Monroy, W. Wu, J. Lin, R.M. Espinosa-Marzal, S.A. Boppart, W.-T. Liu, T.H. Nguyen, Effect of divalent ions and a polyphosphate on composition, structure, and stiffness of simulated drinking water biofilms, npj Biofilms and Microbiomes 4 (1) (2018).
[45] H.K. Kuramitsu, Virulence factors of mutans streptococci: role of molecular genetics, Crit. Rev. Oral Biol. Med. 4 (2) (1993) 159–176.
[46] A.F. Chen, C.B. Wessel, N. Rao, Staphylococcus aureus screening and decolonization in orthopaedic surgery and reduction of surgical site infections, Clin. Orthop. Relat. Res. 471 (7) (2013) 2383–2399.
[47] N.J. Lin, Biofilm over teeth and restorations: what do we need to know? Dent. Mater. 33 (6) (2017) 667–680.
[48] H. Koo, R.N. Allan, R.P. Howlin, P. Stoodley, L. Hall-Stoodley, Targeting microbial biofilms: current and prospective therapeutic strategies, Nat. Rev. Microbiol. 15 (12) (2017) 740–755.
[49] D.G. Moussa, C. Aparicio, Targeting the oral plaque microbiome with immobilized anti-biofilm peptides at tooth-restoration interfaces, PLoS One 15 (7) (2020), e0235283.
[50] Y. Noiri, A. Ehara, T. Kawahara, N. Takemura, S. Ebisu, Participation of bacterial biofilms in refractory and chronic periapical periodontitis, J. Endod. 28 (10) (2002) 679–683.
[51] T. Takeshita, M. Yasui, Y. Shibata, M. Furuta, Y. Saeki, N. Eshima, Y. Yamashita, Dental plaque development on a hydroxyapatite disk in young adults observed by using a barcoded pyrosequencing approach, Sci. Rep. 5 (1) (2015) 8136.
[52] V.S.M. Almeida, J. Azevedo, H.F. Leal, A.T.L. Queiroz, H.P. da Silva Filho, J. N. Reis, Bacterial diversity and prevalence of antibiotic resistance genes in the oral microbiome, PLoS One 15 (9) (2020), e0239664.
[53] Y.K. Lim, S.N. Park, J.H. Shin, Y.H. Chang, Y. Shin, J. Paek, H. Kim, J.K. Kook, Streptococcus periodonticum sp. nov., isolated from human subgingival dental plaque of periodontitis lesion, Curr. Microbiol. 76 (7) (2019) 835–841.
[54] A. Ogawa, S. Furukawa, S. Fujita, J. Mitobe, T. Kawarai, N. Narisawa, T. Sekizuka, M. Kuroda, K. Ochiai, H. Ogihara, S. Kosono, S. Yoneda, H. Watanabe, Y. Morinaga, H. Uematsu, H. Senpuku, Inhibition of Streptococcus mutans biofilm formation by Streptococcus salivarius FruA, Appl. Environ. Microbiol. 77 (5) (2011) 1572–1580.
[55] M. Fan, J. Yang, H.H.K. Xu, M.D. Weir, S. Tao, Z. Yu, Y. Liu, M. Li, X. Zhou, K. Liang, J. Li, Remineralization effectiveness of adhesive containing amorphous calcium phosphate nanoparticles on artificial initial enamel caries in a biofilm-challenged environment, Clin. Oral Invest. (2021).
[56] H.J. Kim, H.E. Bae, J.E. Lee, I.S. Park, H.G. Kim, J. Kwon, D.S. Kim, Effects of bioactive glass incorporation into glass ionomer cement on demineralized dentin, Sci. Rep. 11 (1) (2021) 7016.
[57] J.L. Harding, M.D. Krebs, Controlled and tunable biomimetic apatite mineralization of synthetic hydrogels, Macromol. Mater. Eng. 301 (10) (2016) 1172–1180.
[58] Y.C. Fredholm, N. Karpukhina, D.S. Brauer, J.R. Jones, R.V. Law, R.G. Hill, Influence of strontium for calcium substitution in bioactive glasses on degradation, ion release and apatite formation, J. R. Soc. Interface 9 (70) (2012) 880–889.
[59] M. Du, Q. Li, J. Chen, K. Liu, C. Song, Design and characterization of injectable abalone shell/calcium sulfate bone cement scaffold for bone defect repair, Chem. Eng. J. 420 (2021) 129866.
[60] V. Dusevich, J.R. Melander, J.D. Eick, H. Schatten, SEM in dental research, in: Scanning Electron Microscopy for the Life Sciences, 2012, pp. 211–235.
[61] Y.C. Fredholm, N. Karpukhina, D.S. Brauer, J.R. Jones, R.V. Law, R.G. Hill, Influence of strontium for calcium substitution in bioactive glasses on degradation, ion release and apatite formation, J. R. Soc. Interface 9 (70) (2012) 880–889.
[62] M. Mozafari, S. Banijamali, F. Baino, S. Kargozar, R.G. Hill, Calcium carbonate: adored and ignored in bioactivity assessment, Acta Biomater. 91 (2019) 35–47.
[63] Y.-C. Chiang, H.-J. Chen, H.-C. Liu, S.-H. Kang, B.-S. Lee, F.-H. Lin, H.-P. Lin, C.-P. Lin, A novel mesoporous biomaterial for treating dentin hypersensitivity, J. Dent. Res. 89 (3) (2010) 236–240.
[64] N. Ongphichetmetha, A. Lertpimonchai, C. Champaiboon, Bioactive glass and arginine dentifrices immediately relieved dentine hypersensitivity following non-surgical periodontal therapy: a randomized controlled trial, J. Periodontol. (2021).
[65] M. Garcés-Ortíz, C. Ledesma-Montes, J. Reyes-Gasga, Scanning electron microscopic study on the fibrillar structures within dentinal tubules of human dentin, J. Endod. 41 (9) (2015) 1510–1514.
[66] L.-N. Niu, W. Zhang, D.H. Pashley, L. Breschi, J. Mao, J.-H. Chen, F.R. Tay, Biomimetic remineralization of dentin, Dent. Mater. 30 (1) (2014) 77–96.
[67] R. Alsanea, S. Ravindran, M.I. Fayad, B.R. Johnson, C.S. Wenckus, J. Hao, A. George, Biomimetic approach to perforation repair using dental pulp stem cells and dentin matrix Protein 1, J. Endod. 37 (8) (2011) 1092–1097.
[68] I.J. Davis, C. Wallis, O. Deusch, A. Colyer, L. Milella, N. Loman, S. Harris, A cross-sectional survey of bacterial species in plaque from client owned dogs with healthy gingiva, gingivitis or mild periodontitis, PLoS One 8 (12) (2013), e83158.
[69] L.J. Holcombe, N. Patel, A. Colyer, O. Deusch, C. O'Flynn, S. Harris, Early canine plaque biofilms: characterization of key bacterial interactions involved in initial colonization of enamel, PLoS One 9 (12) (2014), e113744.
[70] P.D. Marsh, D.A. Head, D.A. Devine, Dental plaque as a biofilm and a microbial community—implications for treatment, J. Oral Biosci. 57 (4) (2015) 185–191.
[71] N.H. Lee, M.S. Kang, T.H. Kim, D.S. Yoon, N. Mandakhbayar, S.B. Jo, H.S. Kim, J. C. Knowles, J.H. Lee, H.W. Kim, Dual actions of osteoclastic-inhibition and osteogenic-stimulation through strontium-releasing bioactive nanoscale cement imply biomaterial-enabled osteoporosis therapy, Biomaterials 276 (2021) 121025.
[72] C. Chen, M.D. Weir, L. Cheng, N.J. Lin, S. Lin-Gibson, L.C. Chow, X. Zhou, H.H. K. Xu, Antibacterial activity and ion release of bonding agent containing amorphous calcium phosphate nanoparticles, Dent. Mater. 30 (8) (2014) 891–901.
[73] C.L. Camire, S.J. Saint-Jean, C. Mochales, P. Nevsten, J.S. Wang, L. Lidgren, I. McCarthy, M.P. Ginebra, Material characterization and in vivo behavior of silicon substituted alpha-tricalcium phosphate cement, J. Biomed. Mater. Res. B Appl. Biomater. 76 (2) (2006) 424–431.
[74] C.A. Schneider, W.S. Rasband, K.W. Eliceiri, NIH Image to ImageJ: 25 years of image analysis, Nat. Methods 9 (7) (2012) 671–675.
[75] A. Guentsch, M.D. Fahmy, C. Wehrle, S. Nietzsche, J. Popp, D.C. Watts, S. Kranz, C. Krafft, B.W. Sigusch, Effect of biomimetic mineralization on enamel and dentin: a Raman and EDX analysis, Dent. Mater. 35 (9) (2019) 1300–1307.
[76] X. Li, J. De Munck, K. Yoshihara, M. Pedano, K. Van Landuyt, Z. Chen, B. Van Meerbeek, Re-mineralizing dentin using an experimental tricalcium silicate cement with biomimetic analogs, Dent. Mater. 33 (5) (2017) 505–513.
[77] Ø. Hammer, D.A. Harper, P.D. Ryan, PAST: paleontological statistics software package for education and data analysis, Palaeontol. Electron. 4 (1) (2001) 9.
[78] P. Dixon, VEGAN, a package of R functions for community ecology, J. Veg. Sci. 14 (6) (2003) 927–930.